The paracaspase MALT1 controls cholesterol homeostasis in glioblastoma stem-like cells through lysosome proteome shaping

Clément Maghe, Kilian Trillet, Gwennan André-Grégoire, Mathilde Kerhervé, Laura Merlet, Kathryn Jacobs, Kristine Schauer, Nicolas Bidère, Julie Gavard

To cite this version:

Clément Maghe, Kilian Trillet, Gwennan André-Grégoire, Mathilde Kerhervé, Laura Merlet, et al.. The paracaspase MALT1 controls cholesterol homeostasis in glioblastoma stem-like cells through lysosome proteome shaping. Cell Reports, 2024, 43 (1), pp.113631. 10.1016/j.celrep.2023.113631. hal-04391371

Cell Reports

Report

The paracaspase MALT1 controls cholesterol homeostasis in glioblastoma stem-like cells through lysosome proteome shaping

Graphical abstract

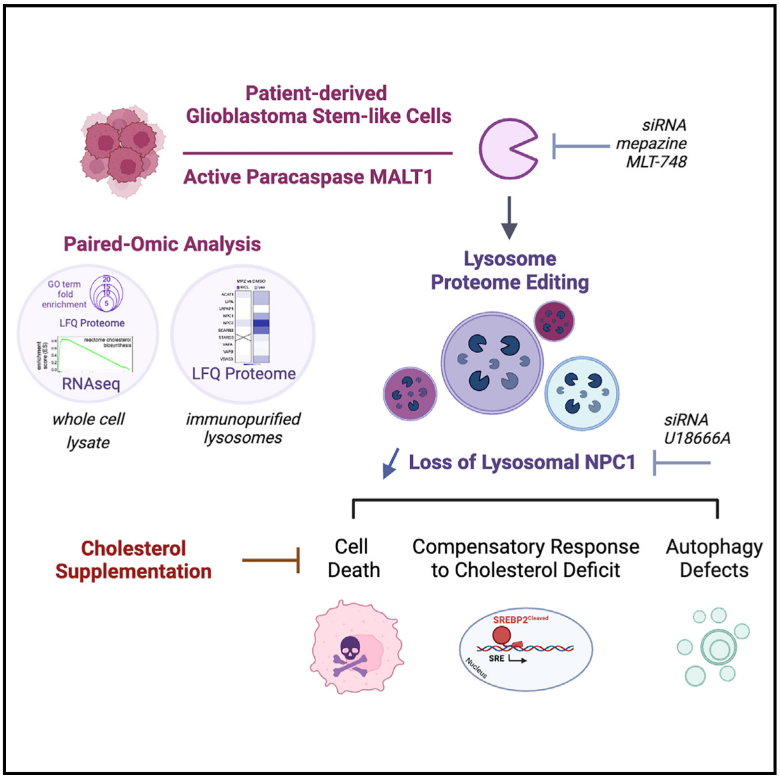

Highlights

- Matched-omic approach shows that the paracaspase MALT1 adjusts cholesterol level
- MALT1 blockage causes cholesterol sequestration in supernumerary lysosomes
- MALT1 prevents cholesterol transporter exhaustion and lysosomal proteome editing
- The targeting of NPC1 abrogates glioblastoma cell viability

Authors

Clément Maghe, Kilian Trillet,
Gwennan André-Grégoire, ...,
Kristine Schauer, Nicolas Bidère,
Julie Gavard

Correspondence

julie.gavard@inserm.fr

In brief

Maghe et al. found that MALT1 inhibition reshapes the lysosomal proteome and lowers NPC1 and NPC2 transporters. This leads to cholesterol sequestration in lysosomes and activates the SREBP2 transcription factor, ultimately decreasing glioblastoma cell growth *in vitro* and *in vivo*, emphasizing their reliance on cholesterol balance.

Maghe et al., 2024, Cell Reports *43*, 113631
January 23, 2024 © 2023 The Author(s).
https://doi.org/10.1016/j.celrep.2023.113631

CellPress

Cell Reports

CellPress
OPEN ACCESS

Report

The paracaspase MALT1 controls cholesterol homeostasis in glioblastoma stem-like cells through lysosome proteome shaping

Clément Maghe,[1,2] Kilian Trillet,[1,2] Gwennan André-Grégoire,[1,2,3] Mathilde Kerhervé,[1,2] Laura Merlet,[1,2]
Kathryn A. Jacobs,[1,2] Kristine Schauer,[4] Nicolas Bidère,[1,2] and Julie Gavard[1,2,3,5,*]
[1]Team SOAP, CRCI2NA, Nantes Université, INSERM, CNRS, Université d'Angers, 44000 Nantes, France
[2]Equipe Labellisée Ligue Nationale Contre le Cancer, 75013 Paris, France
[3]Institut de Cancérologie de l'Ouest (ICO), 44800 Saint-Herblain, France
[4]Institut Gustave Roussy, Université Paris-Saclay, INSERM, CNRS, 94800 Villejuif, France
[5]Lead contact
*Correspondence: julie.gavard@inserm.fr
https://doi.org/10.1016/j.celrep.2023.113631

SUMMARY

Glioblastoma stem-like cells (GSCs) compose a tumor-initiating and -propagating population remarkably vulnerable to variation in the stability and integrity of the lysosomal compartment. Previous work has shown that the expression and activity of the paracaspase MALT1 control GSC viability via lysosome abundance. However, the underlying mechanisms remain elusive. By combining RNA sequencing (RNA-seq) with proteome-wide label-free quantification, we now report that MALT1 repression in patient-derived GSCs alters the homeostasis of cholesterol, which accumulates in late endosomes (LEs)-lysosomes. This failure in cholesterol supply culminates in cell death and autophagy defects, which can be partially reverted by providing exogenous membrane-permeable cholesterol to GSCs. From a molecular standpoint, a targeted lysosome proteome analysis unraveled that Niemann-Pick type C (NPC) lysosomal cholesterol transporters are diluted when MALT1 is impaired. Accordingly, we found that NPC1/2 inhibition and silencing partially mirror MALT1 loss-of-function phenotypes. This supports the notion that GSC fitness relies on lysosomal cholesterol homeostasis.

INTRODUCTION

Glioblastoma (GB) is the most common and aggressive primary brain tumor in adults, with a median survival rate of around 15 months.[1,2] This aggressiveness can be ascribed to the tumor-initiating and -propagating potential of a subpopulation of cells harboring stem properties, referred to as GB stem-like cells (GSCs).[3,4] A growing body of literature now suggests that an intrinsic and tight regulation of the lysosomes is required for sustaining GSC stemness capacities and viability.[5–7] Accordingly, breaking the lysosomal homeostasis has proven efficient in halting GSC growth and triggering GB decline.[5,6]

Lysosomes play crucial roles in nutrient and lipid sensing,[8–11] as they contribute to the spreading of lipids and cholesterol in intracellular membranes.[12,13] Mutations in the lysosomal cholesterol transporters Niemann-Pick type C 1 (NPC1) and NPC2 provoke abnormal accumulation of cholesterol in the lumen and the limiting membrane of lysosomes, which may ultimately impair neuronal functionalities and culminate in mild-to-severe neurological defects in NPC diseases.[14,15] However, the putative roles of NPC1/2 in brain cancer were not examined.

The level of cholesterol is regulated through multiple checkpoints,[16] among which is the sterol regulatory element-binding protein-2 (SREBP2) transcription factor. For instance, SREBP2 governs the expression of proteins and enzymes involved in *de novo* cholesterol synthesis and uptake to counteract cellular cholesterol deficits.[16,17] Counterbalancing mechanisms, such as the down-regulation of the ABC (ATP binding cassette) family exporters via the inhibition of LXR (liver X receptor) and RXR (retinoid X receptor) transcription factors,[16,18] concomitantly occur. Despite these intricate regulatory pathways being explored in other cancers,[19] their implications in GB have mostly been limited to *in silico* analysis and expression patterns.[20–22] Nonetheless, lowering intracellular cholesterol concentration by LXR activation was reported to be lethal to GB cells.[23] However, further description is needed to clarify the dependency of GSCs on cholesterol availability.

Recently, we demonstrated that the paracaspase MALT1, an arginine protease previously linked to lymphocyte activation and signaling downstream of G protein-coupled receptors and receptor tyrosine kinases,[24] regulates GSC viability by maintaining lysosome abundance.[5] However, how precisely MALT1 operates on the lysosome compartment remains unknown. By combining RNA sequencing (RNA-seq) and quantitative proteomic analysis, we now report that the repression of MALT1 activity provokes the dearth in the lysosome loading of cholesterol

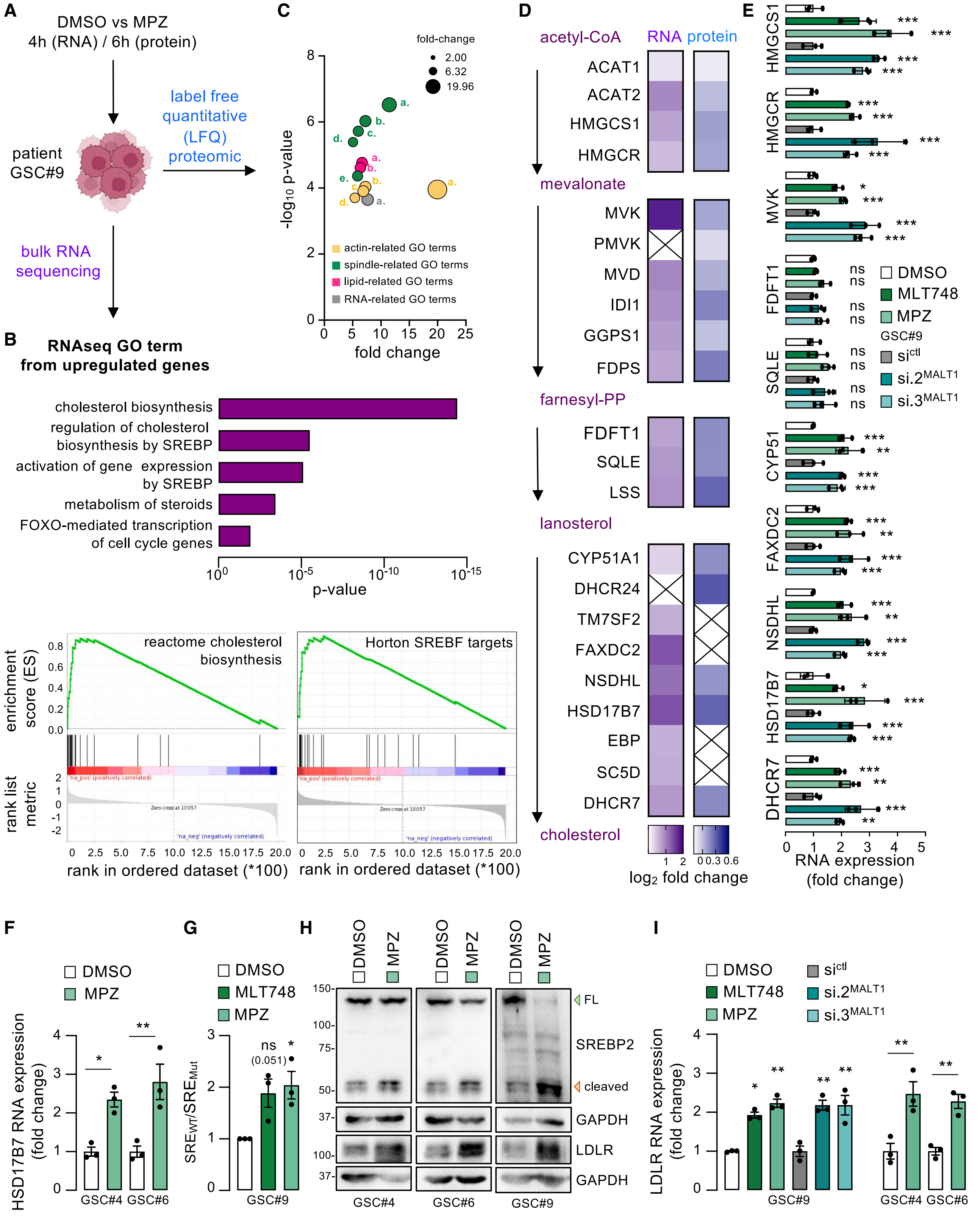

(legend on next page)

transporters. Disrupting intracellular cholesterol trafficking by modifying the lysosome compartment might therefore represent a promising opportunity for GSC eradication.

RESULTS

The inhibition of MALT1 triggers the SREBP2 transcriptional program in GSCs

To investigate the molecular basis for MALT1 influence on the late endosome (LE)-lysosome fitness,[5,25] a dual approach of RNA-seq and proteome-wide label-free quantification (LFQ) analysis was conducted in patient-derived GSCs treated with the MALT1 inhibitor mepazine[26] (Figures 1A, S1A, and S1B). The terms "cholesterol biosynthesis," "regulation of cholesterol biosynthesis by SREBP," and "metabolism of steroids" emerged as the top up-regulated pathways identified within the previously published RNA-seq dataset[5] (Figure 1B; GEO: GSE139018). This enrichment of mRNA akin to cholesterol-related genes was confirmed through gene set enrichment analysis, underscoring cholesterol-associated signatures (Figure 1B). Accordingly, the proteomic analysis highlighted an over-representation of proteins related to the "lipid" node, in addition to "spindle," "actin," and "RNA" associated networks (Figure 1C; Tables S1 and S2; ProteomeXchange: PXD040862). Given that *de novo* cholesterol synthesis occurs primarily through the mevalonate pathway,[28] we next compared the level of transcripts and proteins involved in this metabolic arm (Figure 1D). Remarkably, most of the enzymes identified with this dual-omic approach were increased when MALT1 was inhibited (Figure 1D). This effect was further validated at the RNA level for 8 out of 10 enzymes upon MALT1 pharmacological inhibition with two compounds (mepazine and MLT748)[26,29] (Figure 1E). Of note, mepazine treatment did not alter the expression of MALT1 in patient-derived GSCs (Figure S1C). MALT1 silencing by RNA interference with two independent duplexes yielded similar responses (Figures 1E and S1D). We also validated these results on the HSD17B7 (hydroxysteroid dehydrogenase 17B7) target in two additional patient-derived GSCs (Figure 1F).

Most of these enzymes are under the control of the SREBP2 transcription factor, which shuttles from the endoplasmic reticulum (ER) to the nucleus upon processing and activation (Figure S2A).[30,31] Interestingly, we found that MALT1 inhibition caused a 2-fold increase in the SREBP2 promoter activity (Figure 1G). Furthermore, data mining in TCGA database uncovered correlation between SREBP2 expression level and probability of survival in patients with GB. In fact, SREBP2, but not SREBP1, appeared significantly less expressed in GB samples (Figures S1E and S1F). Western blot analysis revealed SREBP2 processing upon mepazine treatment in three patient-derived GSCs, albeit with variable intensities (Figures 1H and S2B). Moreover, the pharmacological inhibition of MALT1 or its silencing led to an increased expression, both at the mRNA and protein levels, of LDLR (low density lipoprotein receptor), the primary entry road for extracellular cholesterol and a canonical SREBP2 target[12] (Figures 1H, 1I, and S2B). Additionally, chromatin immunoprecipitation (ChIP)-qPCR of mepazine-challenged GSCs confirmed the activation of endogenous SREBP2 transcription factor (Figure S2C). Both drugs and small interfering RNA (siRNA) had minimal to no effect on the levels of SREBP1 canonical targets, including DGAT1 (diacylglycerol acyltransferase 1), SCD1 (stearoyl-coA desaturase-1), and ACLY (ATP citrate lyase), in contrast to the enhanced expression of FASN (fatty acid synthase) (Figure S2D), suggesting that there may be distinct responses in lipid-metabolism-related genes to MALT1 modulation. Taken together, these results indicate that targeting MALT1 preferentially activates the SREBP2 transcriptional program in GSCs, culminating in the expression of the enzymes involved in the synthesis and uptake of cholesterol.

We next examined whether MALT1 inhibition/silencing provoked alterations in intracellular cholesterol concentration and/or its handling in GSCs (Figure S2E). First, we observed that MALT1 silencing resulted in elevated cholesterol concentration in cell lysates (Figure S2F). Likewise, staining with the fluorescent cholesterol probe filipin-III was increased in response to MALT1 inhibition and silencing as assessed by flow cytometry and confocal microscopy (Figures S2G and S2H), suggesting an overall rise in cholesterol content. We also found that MALT1-silenced GSCs significantly accumulated more LDL, one mechanism for transferring cholesterol (Figure S2I). The same was true with mepazine and MLT748. In contrast, MALT1 inhibition strongly reduced the expression of the cholesterol exporters ABCA1 and ABCG1[16] (Figure S2J). Hence, suppressing MALT1 caused GSCs to deploy an arsenal of strategies to increase total cholesterol concentration via synthesis and uptake while reducing its export.

Figure 1. The inhibition of MALT1 triggers the SREBP2 transcriptional program in GSCs

(A–D) Patient-derived glioblastoma stem-like cell GSC#9 received vehicle (DMSO) or MALT1 inhibitor (MPZ; 20 μM).

(A) Workflow of the dual RNA-seq transcriptomic (n = 3) and LFQ proteomic (n = 4) approach.

(B) (Top) REAC enrichment analysis of the top upregulated pathways from RNA-seq. (Bottom) Upregulated genes (fold change > 1.5) analyzed for gene set enrichment analysis (GSEA).

(C) Differentially upregulated proteins analyzed with Pantherdb.[27] GO terms are in Table S1.

(D) Heatmap of cholesterol synthesis pathway genes and proteins expression. Cross: non-identified hits.

(E) RT-qPCR analysis of the indicated targets in GSC#9 treated for 4 h with DMSO, MPZ (20 μM), and MLT748 (5 μM). Alternatively, cells received non-silencing (si^{ctl}) and two duplexes targeting MALT1 (si^{MALT1}) for 3 days. Data were normalized to housekeeping genes (HPRT1, ACTB).

(F) RT-qPCR analysis of HSD17B7 in the indicated GSCs treated as in (E).

(G) SREBP2 reporter activity was evaluated in GSC#9 treated for 16 h with DMSO, MPZ (20 μM), and MLT748 (5 μM).

(H) Western blot analysis of SREBP2 and LDLR in the indicated GSCs treated for 3 and 24 h, respectively, with DMSO and MPZ (20 μM). Green and red arrowheads: FL (full length) and cleaved SREBP2, respectively.

(I) RT-qPCR analysis of LDLR in the indicated GSCs treated as in (E).

All images are representative of n = 3 unless otherwise specified. t test and ANOVA, $*p < 0.05$, $**p < 0.01$, and $***p < 0.001$.

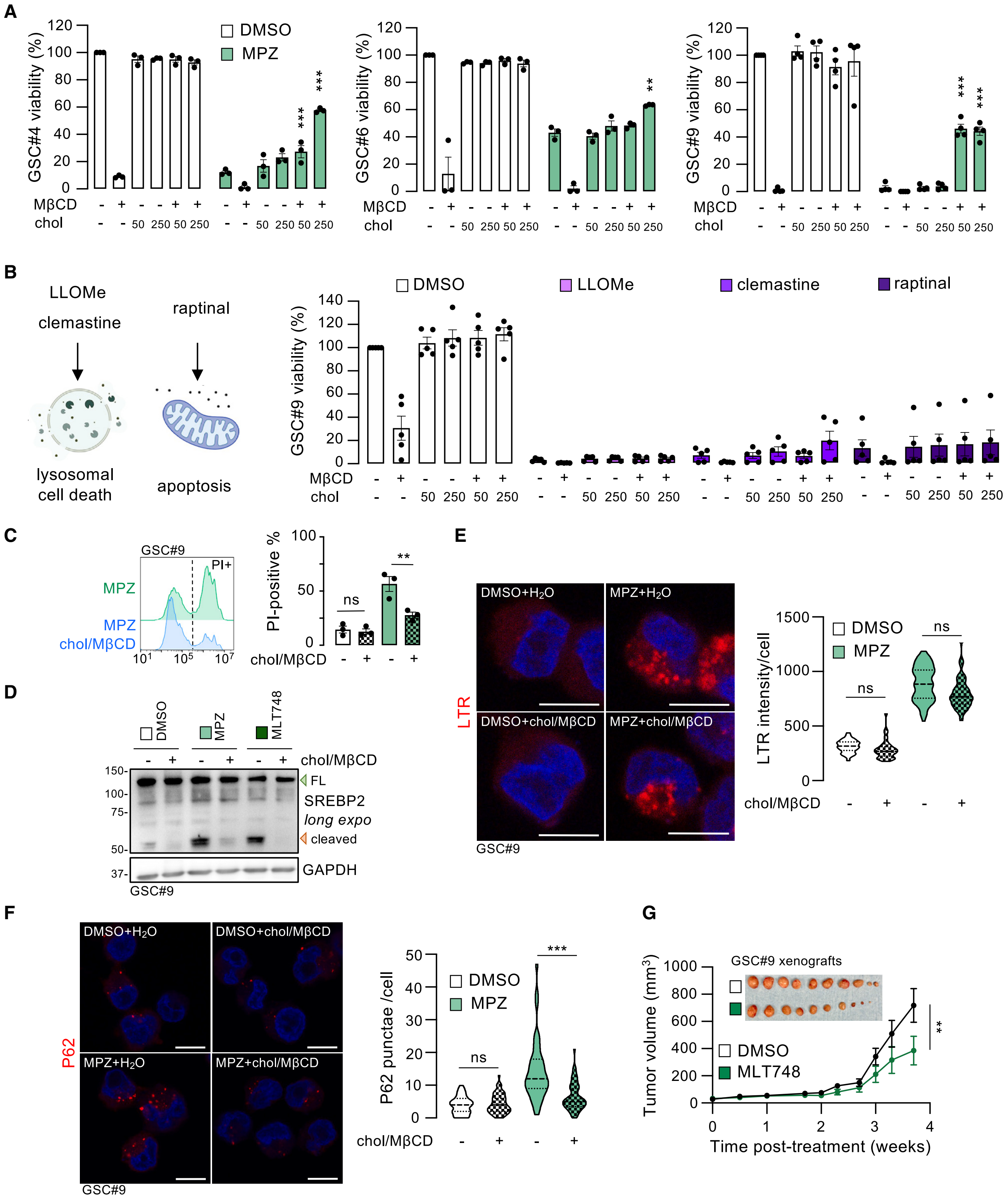

Figure 2. Bioavailable cholesterol partially counteracts MALT1-inhibition-induced cell death

(A) Cell viability in the indicated GSCs pretreated with DMSO and MPZ (20 μM, 1 h) and challenged for 48 h with vehicle (H_2O), MβCD (0.1%), and either cholesterol alone (50 and 250 μM) or in complex with MβCD (chol/MβCD) (n ≥ 3).

(legend continued on next page)

Bioavailable cholesterol partially counteracts MALT1-inhibition-induced loss of cell viability

We next explored whether cell death resulting from MALT1 inhibition[5] could be attributed to SREBP2 activation. As anticipated, SREBP2 silencing precluded the mepazine-associated increase in LDLR abundance (Figure S3A). However, the loss of cell viability caused by mepazine was further augmented upon SREBP2 silencing (Figure S3B). Similar results were obtained with cerivastatin-induced inhibition of HMGCR (3-hydroxy-3-methyl-glutaryl-coA reductase), the rate-limiting enzyme in the cholesterol biosynthetic pathway[32] (Figure S3C). Autophagy obstruction, as illustrated by the accumulation of P62 and LC3B lipidation, was also exacerbated when MALT1 and SREBP2 were inhibited and silenced, respectively (Figures S3D and S3E). Conversely, SREBP2 siRNA alone was not sufficient to drive loss of cell viability and autophagy defects in GSCs (Figures S3B, S3D, and S3E).

Given that SREBP2 silencing aggravated the MALT1-based drop in cell viability, we postulated that GSCs encountered a defective distribution of intracellular cholesterol, despite its apparent global accumulation. To challenge this hypothesis, cell viability was estimated in mepazine-treated GSCs upon cholesterol feeding with free or membrane-permeable MβCD-coupled cholesterol.[17] As expected, the depletion of cellular cholesterol with MβCD alone killed GSCs (Figure 2A). MβCD-coupled cholesterol significantly rescued mepazine-treated GSCs, while free cholesterol did not, across three patient-derived GSCs (Figure 2A). By contrast, astrocytes and brain endothelial cells remained unaffected by mepazine and cholesterol treatments (Figure S3F). Moreover, cholesterol similarly restored GSC viability when cultured in serum-free, complete-serum-, and delipidated-serum-containing media (Figure S3F). However, neither free nor complexed cholesterol protected GSCs from cell loss driven by lysosomal-destabilizing drugs (LLOMe [L-leucyl-L-leucine methyl ester] and clemastine[6]) and a mitochondrial-mediated intrinsic apoptosis activator (raptinal[33]) (Figure 2B), suggesting that cholesterol supplementation selectively counteract MALT1 inhibition. Flow cytometry analysis of propidium iodide incorporation further demonstrated that cholesterol feeding robustly rescued GSCs from mepazine-induced death (Figure 2C). Functionally, the levels of SREBP2 cleavage and of its downstream target LDLR were restored upon cholesterol feeding in MALT1-inhibited GSCs (Figures 2D and S3G). Taken together, these data demonstrated that bioavailable cholesterol rescued cells exposed to MALT1 inhibition.

We then explored how cholesterol supplementation may operate given that MALT1 inhibition caused an aberrant organization in the LE-lysosome compartment[5] (Figure S3H). First, we found that MALT1 remained outside of the LE-lysosome-enriched fractions in control- and mepazine-treated GSCs (Figures S3I and S3J). Moreover, MALT1 remained inhibited by mepazine and MLT748 in the presence of exogenous cholesterol, as visualized by the cleavage of its substrate HOIL1[34] (Figure S3G), suggesting that cholesterol did not directly alter either MALT1 activity or its pharmacological inhibition.

Next, while the abundance of the lysosomal proteins LAMP2 (lysosomal-associated membrane protein 2) and TMEM192 and the LysoTracker signal intensities was not normalized upon cholesterol addition, it did alleviate autophagic defects (Figures 2E, 2F, and S3K). Hence, P62 accumulation and, to a lesser extent, LC3B lipidation were reduced upon cholesterol addition in the context of MALT1 inhibition (Figures 2F and S3L). This suggests that an exogenous source of permeable cholesterol might circumvent lysosome-based defects but not the upstream deregulation of the LEs-lysosomes. The importance of MALT1 in tumor cell expansion was investigated in patient-derived GSC#9 xenografts. Similar to mepazine challenge,[5] MLT748 significantly reduced tumor burden (Figure 2G).

MALT1 inhibition edits the lysosomal proteome and affects the lysosomal cholesterol export machinery

Because exogenous cholesterol retrieved several phenotypes resulting from MALT1 blockade, we next investigated whether lysosomes correctly convey cholesterol[9,35–37] when MALT1 activity and expression were repressed. To this end, lysosomes were immunopurified (lysosome IP [LysoIP][38]) from GSCs stably expressing hemagglutinin (HA)- and FLAG-tagged lysosomal protein TMEM192 (referred to as HA-lyso and FLAG-lyso, respectively; Figures 3A–3C). FLAG-lyso cells served as control cells for anti-HA LysoIP. LysoIP resulted in the enrichment of the lysosomal compartment, as confirmed by the presence of the lysosomal membrane proteins LAMP2 and NPC1, while proteins typical of other organelles were absent (Figure 3D). A portion of the Golgi protein GM130 was, however, trapped in these fractions.

The lysosomal proteomes from vehicle- and mepazine-treated GSCs were then inspected by LFQ (Figure 3A; ProteomeXchange: PXD040855). This unveiled a strong enrichment in lysosomal proteins with few confounding proteins (Table S3). Unlike proteins resident in other organelles, lysosomal proteins were significantly increased in LysoIP samples compared to whole-cell lysates (Figures 3E, 3F, S4A, and S4B). The proteome analysis highlighted autophagy defects in mepazine-treated GSCs, with a substantial accumulation of the classical autophagic

---

(B) Schematic representation of the lysosomal-destabilizing (LLOMe, 1 μM, 1 h, and clemastine, 20 μM, 1 h) and pro-apoptotic (raptinal, 2 μM, 1 h) drugs used. Cell viability as in (A) (n = 5).

(C) Propidium iodide (PI) incorporation by flow cytometry in GSC#9 as in (A).

(D) Western blot analysis of SREBP2 in GSC#9 pretreated for 1 h with DMSO, MPZ (20 μM), and MLT748 (5 μM) and challenged for 3 h with H_2O and chol/MβCD (250 μM). Green and red arrowheads: FL and cleaved SREBP2, respectively.

(E and F) Confocal analysis of LysoTracker (LTR; E) and P62 (F) staining in GSC#9 pretreated for 1 h with DMSO and MPZ (20 μM) and challenged for 16 h with H_2O and chol/MβCD (250 μM). Scale bar: 10 μm. Violin representations: quantification of LTR intensity/cell ($n > 71$) and P62 punctae/cell ($n > 39$).

(G) Nude mice were implanted with GSC#9 and treated with DMSO or MLT748 (4 mg/kg) daily once tumors were palpable. Tumor volume was measured twice a week. Inset: endpoint tumors (n = 5 mice/group).

All images are representative of n = 3 unless otherwise specified. t test and ANOVA, *$p < 0.05$, **$p < 0.01$, and ***$p < 0.001$.

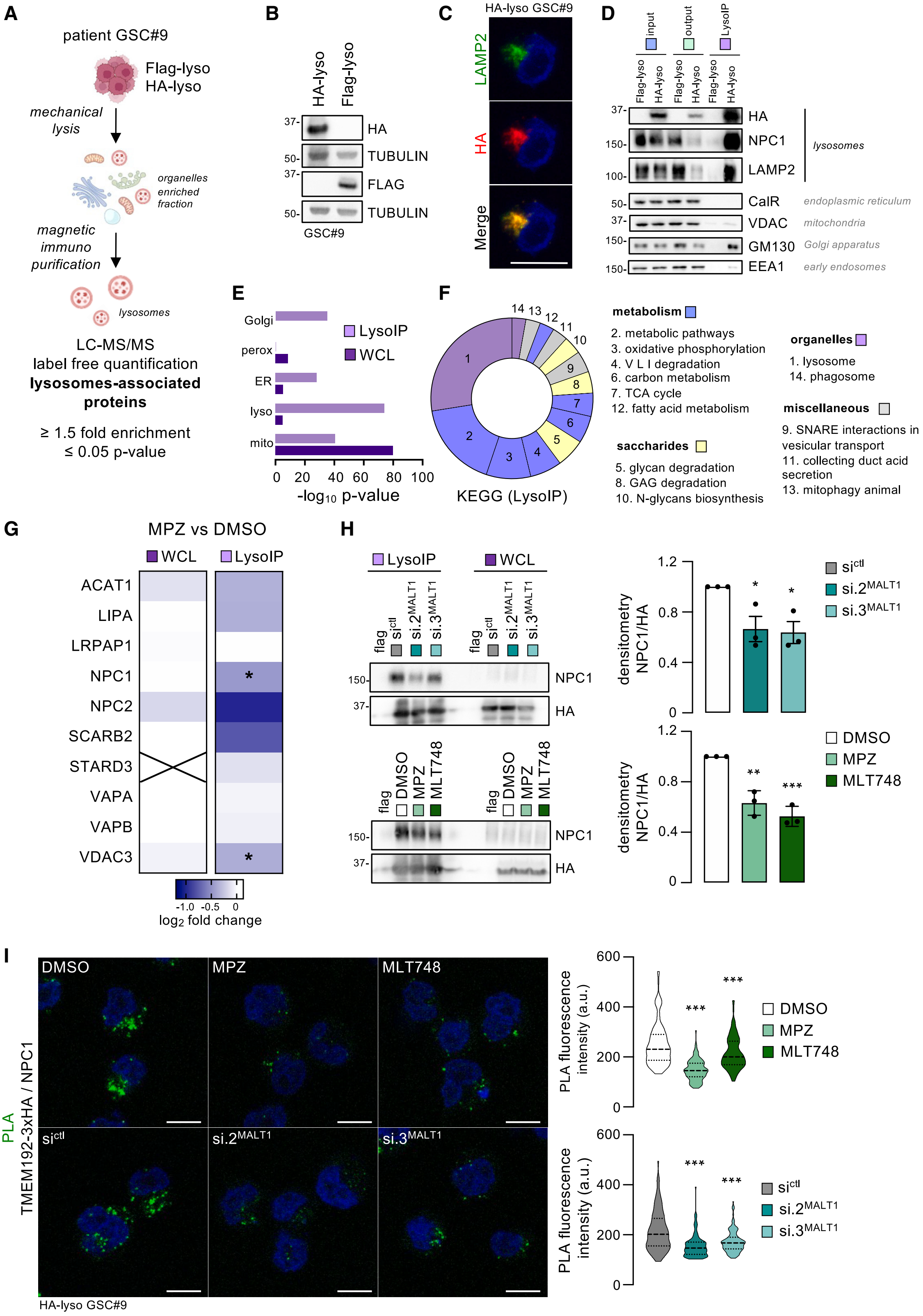

(legend on next page)

receptors TAX1BP1 (Tax1-binding protein 1) and P62 (Figures S4C and S4D). This initial examination of the lysosome proteome supports the notion that MALT1 inhibition leads to a defect in their degradative capacity. A closer exploration into the differentially expressed proteins identified a modest reduction in the levels of most proteins related to cholesterol in lysosomes, like NPC1, NPC2, and SCARB2 (scavenger receptor class B member 2) transporters, while this was not observed in total lysates (Figures 3G and S4D). The mRNA levels of NPC1 and NPC2 were left unchanged in response to MALT1 inhibition and silencing (Figure S4E), indicating a potential shift in the relative repartition of these lysosomal-resident proteins rather than a drop in their expression. This reduced presence of NPC1 in lysosomes was independently validated in cells challenged with MALT1 inhibitors and siRNA (Figure 3H). Indeed, NPC1 was less closely associated with lysosomes, based on confocal analysis and proximity ligation assay (PLA) (Figures 3I and S4F), suggesting a reduction in the number of NPC1-positive lysosomes.

We next explored the role of Quaking (QKI), a K homology domain containing RNA-binding protein, reported to interact with MALT1[5] and SREBP2[39,40] and to downregulate LEs-lysosomes,[5,25] in MALT1-induced phenotypes. QKI silencing negated the effects of MALT1 inhibition on the upregulation of LDLR and HSD17B7 (Figures S5A and S5B). A similar but partial effect of QKI repression was noted on the expression of the cholesterol efflux transporter ABCA1 (Figure S5A). Staining with filipin-III revealed that cholesterol accumulation in mepazine-treated GSCs was attenuated following QKI silencing (Figure S5C). Moreover, LysoIP and PLA assays indicated that the level of NPC1 protein was restored in TMEM192-positive organelles when MALT1 inhibition was combined with QKI silencing (Figures S5D and S5E). Thus, QKI is required for the impaired association of cholesterol transporters with lysosomes, engendered by MALT1 targeting.

NPC1 blockade partially recapitulates MALT1-repressed phenotypes in GSCs

In silico analysis of TGCA showed that low NPC1 RNA expression correlated with a significantly higher probability of survival in patients with GB (Figure S6A). This was, however, not significant for NPC2 (Figure S6B). Patient clustering based on RNA expression levels of both NPC1 and NPC2 highlighted an improved probability of survival for patients with low NPC1/2 RNA expression (Figures 4A and S6C). Moreover, patients with low NPC1/2 expression exhibited higher SREBP2 RNA expression, linked to a higher probability of survival (Figure S6D).

We next explored whether the change in NPC1/lysosome ratio could execute MALT1-related cell death in GSCs. As expected, U18666A, a classical NPC1 inhibitor,[41] promoted substantial SREBP2 processing and LDLR expression[41] (Figure 4B). Likewise, reporter assays indicated that SREBP2 was activated upon NPC1 blockade (Figure 4C). Thus, MALT1 inhibition paralleled both effects of NPC1 inhibition on SREBP2 and LDLR, albeit to a lesser extent. Moreover, cholesterol, as assessed by bioluminescent assay and staining with filipin-III, was globally increased in NPC1-silenced GSCs (Figures 4D–4F). Interestingly, filipin-III-stained cholesterol accumulated in TMEM192-positive lysosomes upon NPC1 inhibition and silencing similarly to cells exposed to MALT1-targeting drugs and siRNA (Figure 4F). The levels of the lipid lysobisphosphatidic acid (LBPA), which significantly accumulates in NPC1-inhibited cells,[42] were also augmented with the repression of MALT1 (Figure 4G). This indicates shared responses to MALT1 and NPC1 suppression in GSCs, albeit with varying amplitude. However, hindering NPC1 and NPC2 did not recapitulate the lysosomal increase observed when MALT1 activity/expression was abrogated (Figures 4H and S6E). The accumulation of the autophagic receptor P62 induced by MALT1 inhibition was nonetheless phenocopied by the use of U18666A (Figure 4H), suggesting that lysosomes from MALT1- and NPC1-inhibited GSCs may feature similar degradative defects. Likewise, U18666A treatment and the silencing of NPC1 and NPC2 significantly reduced GSC viability (Figures 4I, 4J, and S6F). Of note, blocking MALT1 proved more effective at driving cell death than targeting NPC transporters, suggesting possible, additional mediators, such as the number of lysosomes themselves and/or their permeability extent. U18666A was not as toxic in astrocytes and brain endothelial cells (Figures S6F and S6G), recapitulating the neutral impact of mepazine.[5] In line with this, Jurkat and BJAB, T and B lymphocytes, respectively, without intrinsic MALT1 activity were left intact, unlike the MALT1-dependent OCI-Ly3 lymphoma cells[43,44] (Figure S6G), raising the possibility of a causal link between MALT1 activity and sensitivity to U18666A. To evaluate the potential of targeting NPC1 in GB, a xenograft model was revisited with U18666A administration, which significantly reduced plasmatic cholesterol concentration (Figures 4K and 4L). Similar to mepazine[5] and MLT748, tumor growth was lessened, underscoring the importance of lysosomal cholesterol transport for GB growth.

Figure 3. MALT1 edits the lysosomal proteome and affects the lysosomal cholesterol export machinery

(A) LFQ proteomic after anti-HA immunopurification (LysoIP) in GSC#9 stably expressing the lysosomal protein TMEM192 (HA- or FLAG-lyso); fold changes on HA/FLAG ratio (n = 4).

(B and C) Western blot (B) and confocal (C) analysis as indicated in FLAG-lyso and HA-lyso GSC#9. Scale bar: 10 μm.

(D) Western blot analysis as indicated in FLAG-lyso or HA-lyso GSC#9 inputs, outputs, and LysoIP.

(E) GO:CC enrichment analysis from the whole-cell lysate (WCL) and LysoIP proteomics analysis.

(F) KEGG enrichment analysis of lysosome-associated proteins (fold change > 1.5 and $p \leq 0.05$, in HA/FLAG ratio).

(G) Heatmap of KEGG: cholesterol metabolism hits from WCLs and LysoIP in HA-lyso GSC#9 treated with DMSO and MPZ (20 μM, 6 h). Cross: not-identified candidates.

(H) Western blot analysis of NPC1 from FLAG-lyso and HA-lyso GSC#9 LysoIP and WCLs. Top: cells transfected with si^{ctl} and two si^{MALT1} for 3 days. Bottom: cells treated for 6 h with DMSO, MPZ (20 μM), and MLT748 (5 μM). Densitometric analysis of NPC1 level normalized to TMEM192-3xHA (HA).

(I) Confocal analysis of proximity ligation assay (PLA) between TMEM192-3xHA and NPC1. HA-lyso GSC#9 was treated as described in (H). Scale bar: 10 μm. Violin representations: quantification of PLA signal intensity/cell (n > 108).

All images are representative of n = 3 unless otherwise specified. ANOVA, $^{*}p < 0.05$, $^{**}p < 0.01$, and $^{***}p < 0.001$.

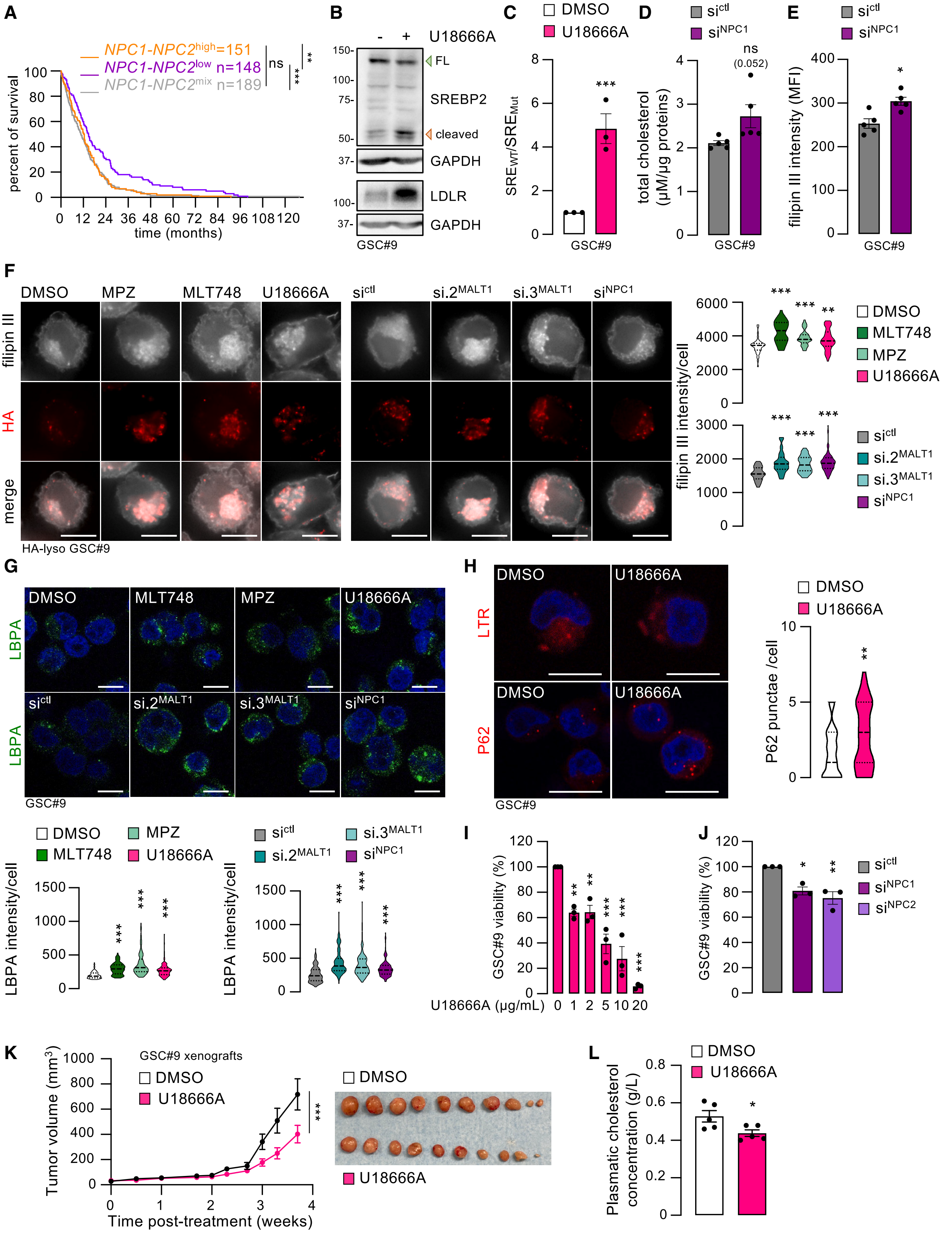

(legend on next page)

DISCUSSION

Taken together, our results lend support to an underestimated role of MALT1 in the regulation of intracellular cholesterol equilibrium. Indeed, suppressing MALT1 activity/expression causes a profound remodeling of the LE-lysosomal compartment, accompanied by the retention of cholesterol and subsequent failure in its intracellular delivery. These defects ultimately culminate in GSCs' demise. Concomitantly to an accumulation of intracellular cholesterol, MALT1-repressed cells deploy a myriad of strategies to cope with cholesterol demands.[16,31] Our results suggest that MALT1-inhibited GSCs launch a compensatory program to counteract cholesterol retention. In a MALT1-suppressed context, hampering SREBP2-mediated cholesterol synthesis with RNA interference or cerivastatin[32] aggravates both autophagy defects and cell death in GSCs. This highlights the strong dependency of these cells on finely tuned cholesterol homeostasis. As U18666A and MLT748 proved efficacy in reducing tumor growth in xenografted mice, combining the targeting of MALT1 and cholesterol supply may therefore represent a valid strategy for GSC eradication. However, one caveat with the canonical use of statins resides in the reported adverse effects on non-tumor cells, like astrocytes.[23,45] Hence, more selective cholesterol-lowering agents may be valuable.[23]

Our data identify that MALT1-inhibited cells experience a deficiency in cholesterol handling, likely due to the reduced levels of cholesterol transporters within lysosomes. We provide evidence that NPC1 abundance is reduced within these organelles while cellular expression remains steady, suggesting that MALT1 inhibition may cause the paucity of cholesterol transporters in lysosomes. Paralleling the situation in NPC patients with mutations in NPC1/2 genes affecting protein folding or ability to anchor in lipid-rich membranes,[46] it is plausible that NPC1 is retained in the ER. Although we cannot rule out its rerouting to different cellular membranes, NPC1 might alternatively become diluted in the pool of newly generated lysosomes. Notably, QKI silencing, which attenuates MALT1-associated lysosomal defects, also mitigates the dispersal of NPC1 from lysosomes. In keeping with this notion, MALT1 silencing might create NPC1-exhausted lysosomes, making the as-produced lysosome population less prone to export cholesterol.[13,36,37] Arguing in favor of the apparition of a pool of dysfunctional NPC1-defective lysosomes, targeted proteomic highlights an autophagy signature. This aligns with previous studies that demonstrated the pronounced autophagic defects in NPC1-null models.[9,47] Overall, the increased abundance of abnormal lysosomes results in a widespread accumulation and sequestration of cholesterol, which subsequently contribute to most of the MALT1-dependent phenotypes.

How exactly the cholesterol inflation in lysosomes leads to cell death remains to be elucidated. Paralleling lysosomal storage diseases, where cholesterol is trapped in lysosomes,[9,37] MALT1 suppression reiterates traits seen in NPC diseases, including the accumulation of cholesterol in lysosomes, lysosomal membrane fragility, and compromised proteolysis capacities.[9,47,48] The resulting cholesterol depletion in other intracellular compartments, the potential disorganization in cellular membranes, and the disassembly of essential signaling pathways could globally weaken cell fitness.[16,21]

Taken together, our data substantiate the notion that the viability of MALT1-active GSCs hinges on effective cholesterol distribution. These cells are ultimately vulnerable to failure in the cholesterol dispatch, as blocking the NPC1 transporter and/or increasing the number of lysosomes as storage sites proves to be lethal.

Limitations of the study

This study did not establish the exact mechanistic link between MALT1 and cholesterol regulation, although several mediator hints were identified (QKI, SREBP2, NPC1). Detailed studies of the lysosomal compartment could help define the precise role of NPC1, notably its influence on ER-lysosome cholesterol transfer as an alternate source besides LDLR uptake. Non-GSC models, such as astrocytes and endothelial cells, were used only with parsimony to control for the effects of MALT1. It will be of paramount importance to next evaluate the role of MALT1 on cholesterol distribution in non-cancer contexts, notably upon MALT1 physiological activation. Ultimately, further research is essential to explore the *in vivo* translation of our discoveries, with a particular focus on understanding the contribution of cholesterol supply and overall homeostasis.

Figure 4. NPC1 blockade partially recapitulated MALT1-repressed phenotypes in GSCs

(A) Kaplan-Meier curve for 488 patients with GB (TCGA Agilent-4502A dataset), grouped based on low (purple), high (orange), or mixed (gray) *NPC1* and *NPC2* mRNA levels. Log-rank p values are indicated.

(B) Western blot analysis of SREBP2 and LDLR in GSC#9 treated for 3 and 24 h, respectively, with DMSO and U18666A (2 μg/mL). Green and red arrowheads: FL and cleaved SREBP2, respectively.

(C) SREBP2 reporter activity in GSC#9 treated as in (B) for 16 h.

(D and E) Total cholesterol level in GSC#9 transfected with si^{ctl} and NPC1-targeting duplexes (si^{NPC1}) for 3 days, measured by bioluminescent assay (ratio cholesterol/proteins, μM/μg, n = 5, D), and estimated with filipin-III flow cytometry (mean fluorescence intensity, n = 5, E).

(F) Confocal analysis of filipin-III and TMEM192-3xHA (HA) staining in HA-lyso GSC#9 treated for 16 h with DMSO, MPZ (20 μM), MLT748 (5 μM), and U18666A (2 μg/mL). Alternatively, cells received si^{ctl}, si^{NPC1}, and si^{MALT1} for 3 days. Scale bar: 10 μm. Violin representations: quantification of filipin-III signal intensity/cell ($n > 38$).

(G and H) Confocal analysis of lysobisphosphatidic acid (LBPA) (G), LTR (H, top), and P62 (H, bottom) in GSC#9 treated as in (F) for 24 h. Scale bar: 10 μm. Violin representations: quantification of LBPA signal intensity/cell (G, $n > 112$) and P62 punctae/cell (H, n = 41).

(I and J) Cell viability was measured in GSC#9 treated for 48 h with DMSO and U18666A at the indicated doses (I). Alternatively, cells were transfected for 3 days with si^{ctl}, si^{NPC1}, and si^{NPC2} (J).

(K and L) Nude mice were implanted with GSC#9 in each flank and treated with either DMSO or U18666A (4 mg/kg) daily once tumors were palpable. Tumor volume was measured twice a week (K, left). Endpoint tumors (K, right) and plasmatic cholesterol at endpoint (L) (n = 5 mice/group).

All images are representative of n = 3 unless otherwise specified. t test and ANOVA, $^{*}p < 0.05$, $^{**}p < 0.01$, and $^{***}p < 0.001$.

STAR★METHODS

Detailed methods are provided in the online version of this paper and include the following:

- KEY RESOURCES TABLE
- RESOURCE AVAILABILITY
  - Lead contact
  - Materials availability
  - Data and code availability
- EXPERIMENTAL MODEL AND STUDY PARTICIPANT DETAILS
  - Animals
  - Cell culture
- METHOD DETAILS
  - Mice xenograft models
  - siRNA transfection
  - Plasmid transfection and lentiviral transduction
  - TCGA analysis
  - Cholesterol/MβCD complexes preparation
  - Cell lysis and western-blots
  - Cellular fractionation
  - Cell viability and cell death assays
  - Immunofluorescence staining
  - Micropatterning
  - Proximity ligation assay (PLA)
  - Confocal analysis
  - Filipin-III staining for imaging and flow cytometry
  - qPCR analysis
  - ChIP-qPCR
  - RNAseq analysis
  - Luciferase SREBP2 reporter assay
  - Cholesterol dosage
  - Lysosome immunoprecipitation (LysoIP)
  - Label-free quantification (LFQ) proteomic processing and analysis of whole cell lysates
  - Label-free quantification (LFQ) proteomic processing and analysis of LysoIP
  - Proteomic and RNAseq enrichment analysis
- QUANTIFICATION AND STATISTICAL ANALYSIS

SUPPLEMENTAL INFORMATION

Supplemental information can be found online at https://doi.org/10.1016/j.celrep.2023.113631.

ACKNOWLEDGMENTS

We are grateful to SOAP team members (CRCI^{2}NA, Nantes, France), especially Agniezska Barbach and Lucas Ottero. We also thank Cédric Broussard, Johanna Bruce, Philippe Chafey, and François Guillonneau, from the Proteom'IC facility, Université Paris Cité, CNRS, INSERM, Institut Cochin, 75014 Paris, France (supported by the DIM Thérapie Génique Paris Ile-de-France Région, IBiSA, and the Labex GR-Ex), for performing sample preparation, acquisition, and analysis. We are also grateful to Cédric Le May, Xavier Prieur, and Thibaud Sotin (L'Institut du Thorax, Nantes, France) for technical advice, as well as to Laetitia Durand and François Paris (CRCI^{2}NA, Nantes, France). We would like to acknowledge the core facilities from UMS Biocore, Nantes, France (MicroPICell, ANR-10-INBS-04 and Cytocell). This work was supported by Fondation ARC contre le Cancer; INCa PLBIO (2019-151, 2019-291, INCa_18384, and INCa PAIR-CEREB INCa_16285); Ligue Nationale Contre le Cancer (EL2022) and Comités Ligue 35, 44, 49, 72, 85; and Région Pays de la Loire. C.M., M.K., and L.M. received a fellowship from Ligue Contre le Cancer and K.A.J. from Fondation ARC contre le Cancer. The team is part of the SIRIC ILIAD (INCa-DGOS-INSERM-ITMO Cancer_18011).

AUTHOR CONTRIBUTIONS

Conception and design, C.M., N.B., and J.G.; data acquisition, C.M., K.T., G.A.-G., M.K., L.M., and K.A.J.; data visualization, C.M.; data analysis, C.M., K.T., G.A.-G., M.K., L.M., K.A.J., N.B., and J.G.; data interpretation, C.M., K.T., G.A.-G., M.K., L.M., K.A.J., K.S., N.B., and J.G.; drafted the article, C.M. and N.B.; wrote the article, J.G.; essential reagents, K.S. All authors approved the manuscript.

DECLARATION OF INTERESTS

The authors declare no competing interests.

Received: March 24, 2023
Revised: November 27, 2023
Accepted: December 13, 2023

REFERENCES

1. Ohgaki, H., and Kleihues, P. (2005). Population-Based Studies on Incidence, Survival Rates, and Genetic Alterations in Astrocytic and Oligodendroglial Gliomas. J. Neuropathol. Exp. Neurol. *64*, 479–489.
2. Stupp, R., Hegi, M.E., Mason, W.P., van den Bent, M.J., Taphoorn, M.J.B., Janzer, R.C., Ludwin, S.K., Allgeier, A., Fisher, B., Belanger, K., et al. (2009). Effects of radiotherapy with concomitant and adjuvant temozolomide versus radiotherapy alone on survival in glioblastoma in a randomised phase III study: 5-year analysis of the EORTC-NCIC trial. Lancet Oncol. *10*, 459–466.
3. Lathia, J.D., Mack, S.C., Mulkearns-Hubert, E.E., Valentim, C.L.L., and Rich, J.N. (2015). Cancer stem cells in glioblastoma. Genes Dev. *29*, 1203–1217.
4. Singh, S.K., Hawkins, C., Clarke, I.D., Squire, J.A., Bayani, J., Hide, T., Henkelman, R.M., Cusimano, M.D., and Dirks, P.B. (2004). Identification of human brain tumour initiating cells. Nature *432*, 396–401.
5. Jacobs, K.A., André-Grégoire, G., Maghe, C., Thys, A., Li, Y., Harford-Wright, E., Trillet, K., Douanne, T., Alves Nicolau, C., Frénel, J.S., et al. (2020). Paracaspase MALT1 regulates glioma cell survival by controlling endo-lysosome homeostasis. EMBO J. *39*, e102030.
6. Le Joncour, V., Filppu, P., Hyvönen, M., Holopainen, M., Turunen, S.P., Sihto, H., Burghardt, I., Joensuu, H., Tynninen, O., Jääskeläinen, J., et al. (2019). Vulnerability of invasive glioblastoma cells to lysosomal membrane destabilization. EMBO Mol. Med. *11*, e9034.
7. Zhou, W., Guo, Y., Zhang, X., and Jiang, Z. (2020). Lys05 induces lysosomal membrane permeabilization and increases radiosensitivity in glioblastoma. J. Cell. Biochem. *121*, 2027–2037.
8. Castellano, B.M., Thelen, A.M., Moldavski, O., Feltes, M., van der Welle, R.E.N., Mydock-McGrane, L., Jiang, X., van Eijkeren, R.J., Davis, O.B., Louie, S.M., et al. (2017). Lysosomal cholesterol activates mTORC1 via an SLC38A9–Niemann-Pick C1 signaling complex. Science *355*, 1306–1311.
9. Davis, O.B., Shin, H.R., Lim, C.-Y., Wu, E.Y., Kukurugya, M., Maher, C.F., Perera, R.M., Ordonez, M.P., and Zoncu, R. (2021). NPC1-mTORC1 Signaling Couples Cholesterol Sensing to Organelle Homeostasis and Is a Targetable Pathway in Niemann-Pick Type C. Dev. Cell *56*, 260–276.e7.
10. Shin, H.R., Citron, Y.R., Wang, L., Tribouillard, L., Goul, C.S., Stipp, R., Sugasawa, Y., Jain, A., Samson, N., Lim, C.-Y., et al. (2022). Lysosomal GPCR-like protein LYCHOS signals cholesterol sufficiency to mTORC1. Science *377*, 1290–1298.

11. Lawrence, R.E., and Zoncu, R. (2019). The lysosome as a cellular centre for signalling, metabolism and quality control. Nat. Cell Biol. *21*, 133–142.
12. Trinh, M.N., Brown, M.S., Goldstein, J.L., Han, J., Vale, G., McDonald, J.G., Seemann, J., Mendell, J.T., and Lu, F. (2020). Last step in the path of LDL cholesterol from lysosome to plasma membrane to ER is governed by phosphatidylserine. Proc. Natl. Acad. Sci. *117*, 18521–18529.
13. Meng, Y., Heybrock, S., Neculai, D., and Saftig, P. (2020). Cholesterol Handling in Lysosomes and Beyond. Trends Cell Biol. *30*, 452–466.
14. Winkler, M.B.L., Kidmose, R.T., Szomek, M., Thaysen, K., Rawson, S., Muench, S.P., Wüstner, D., and Pedersen, B.P. (2019). Structural Insight into Eukaryotic Sterol Transport through Niemann-Pick Type C Proteins. Cell *179*, 485–497.e18.
15. Cariati, I., Masuelli, L., Bei, R., Tancredi, V., Frank, C., and D'Arcangelo, G. (2021). Neurodegeneration in Niemann–Pick Type C Disease: An Updated Review on Pharmacological and Non-Pharmacological Approaches to Counteract Brain and Cognitive Impairment. Int. J. Mol. Sci. *22*, 6600.
16. Luo, J., Yang, H., and Song, B.-L. (2020). Mechanisms and regulation of cholesterol homeostasis. Nat. Rev. Mol. Cell Biol. *21*, 225–245.
17. Radhakrishnan, A., Goldstein, J.L., McDonald, J.G., and Brown, M.S. (2008). Switch-like Control of SREBP-2 Transport Triggered by Small Changes in ER Cholesterol: A Delicate Balance. Cell Metab. *8*, 512–521.
18. Lee, M.-S., and Bensinger, S.J. (2022). Reprogramming cholesterol metabolism in macrophages and its role in host defense against cholesterol-dependent cytolysins. Cell. Mol. Immunol. *19*, 327–336.
19. Beckwitt, C.H., Brufsky, A., Oltvai, Z.N., and Wells, A. (2018). Statin drugs to reduce breast cancer recurrence and mortality. Breast Cancer Res. *20*, 144.
20. Li, D., Li, S., Xue, A.Z., Smith Callahan, L.A., and Liu, Y. (2020). Expression of SREBP2 and cholesterol metabolism related genes in TCGA glioma cohorts. Medicine (Baltim.) *99*, e18815.
21. Huang, B., Song, B.L., and Xu, C. (2020). Cholesterol metabolism in cancer: mechanisms and therapeutic opportunities. Nat. Metab. *2*, 132–141.
22. Lewis, C.A., Brault, C., Peck, B., Bensaad, K., Griffiths, B., Mitter, R., Chakravarty, P., East, P., Dankworth, B., Alibhai, D., et al. (2015). SREBP maintains lipid biosynthesis and viability of cancer cells under lipid- and oxygen-deprived conditions and defines a gene signature associated with poor survival in glioblastoma multiforme. Oncogene *34*, 5128–5140.
23. Villa, G.R., Hulce, J.J., Zanca, C., Bi, J., Ikegami, S., Cahill, G.L., Gu, Y., Lum, K.M., Masui, K., Yang, H., et al. (2016). An LXR-Cholesterol Axis Creates a Metabolic Co-Dependency for Brain Cancers. Cancer Cell *30*, 683–693.
24. Jaworski, M., and Thome, M. (2016). The paracaspase MALT1: biological function and potential for therapeutic inhibition. Cell. Mol. Life Sci. *73*, 459–473.
25. Shingu, T., Ho, A.L., Yuan, L., Zhou, X., Dai, C., Zheng, S., Wang, Q., Zhong, Y., Chang, Q., Horner, J.W., et al. (2017). Qki deficiency maintains stemness of glioma stem cells in suboptimal environment by downregulating endolysosomal degradation. Nat. Genet. *49*, 75–86.
26. Schlauderer, F., Lammens, K., Nagel, D., Vincendeau, M., Eitelhuber, A.C., Verhelst, S.H.L., Kling, D., Chrusciel, A., Ruland, J., Krappmann, D., and Hopfner, K.P. (2013). Structural Analysis of Phenothiazine Derivatives as Allosteric Inhibitors of the MALT1 Paracaspase. Angew. Chem. Int. Ed. *52*, 10384–10387.
27. Mi, H., Muruganujan, A., Huang, X., Ebert, D., Mills, C., Guo, X., and Thomas, P.D. (2019). Protocol Update for large-scale genome and gene function analysis with the PANTHER classification system (v.14.0). Nat. Protoc. *14*, 703–721.
28. Mazein, A., Watterson, S., Hsieh, W.-Y., Griffiths, W.J., and Ghazal, P. (2013). A comprehensive machine-readable view of the mammalian cholesterol biosynthesis pathway. Biochem. Pharmacol. *86*, 56–66.
29. Quancard, J., Klein, T., Fung, S.-Y., Renatus, M., Hughes, N., Israël, L., Priatel, J.J., Kang, S., Blank, M.A., Viner, R.I., et al. (2019). An allosteric MALT1 inhibitor is a molecular corrector rescuing function in an immunodeficient patient. Nat. Chem. Biol. *15*, 304–313.
30. Horton, J.D., Shah, N.A., Warrington, J.A., Anderson, N.N., Park, S.W., Brown, M.S., and Goldstein, J.L. (2003). Combined analysis of oligonucleotide microarray data from transgenic and knockout mice identifies direct SREBP target genes. Proc. Natl. Acad. Sci. *100*, 12027–12032.
31. Horton, J.D., Goldstein, J.L., and Brown, M.S. (2002). SREBPs: activators of the complete program of cholesterol and fatty acid synthesis in the liver. J. Clin. Invest. *109*, 1125–1131.
32. Kuhlmann, J., Mück, W., Bischoff, H., von Keutz, E., and Llewellyn, M. (1998). Cerivastatin (BAY w 6228): A Novel HMG-CoA Reductase Inhibitor. Cardiovasc. Drug Rev. *16*, 236–263.
33. Palchaudhuri, R., Lambrecht, M.J., Botham, R.C., Partlow, K.C., van Ham, T.J., Putt, K.S., Nguyen, L.T., Kim, S.-H., Peterson, R.T., Fan, T.M., and Hergenrother, P.J. (2015). A Small Molecule that Induces Intrinsic Pathway Apoptosis with Unparalleled Speed. Cell Rep. *13*, 2027–2036.
34. Douanne, T., Gavard, J., and Bidère, N. (2016). The paracaspase MALT1 cleaves the LUBAC subunit HOIL1 during antigen receptor signaling. J. Cell Sci. *129*, 1775–1780.
35. Chu, B.-B., Liao, Y.-C., Qi, W., Xie, C., Du, X., Wang, J., Yang, H., Miao, H.-H., Li, B.-L., and Song, B.-L. (2015). Cholesterol transport through lysosome-peroxisome membrane contacts. Cell *161*, 291–306.
36. Lange, Y., Ye, J., and Steck, T.L. (1998). Circulation of Cholesterol between Lysosomes and the Plasma Membrane. J. Biol. Chem. *273*, 18915–18922.
37. Lim, C.-Y., Davis, O.B., Shin, H.R., Zhang, J., Berdan, C.A., Jiang, X., Counihan, J.L., Ory, D.S., Nomura, D.K., and Zoncu, R. (2019). ER–lysosome contacts enable cholesterol sensing by mTORC1 and drive aberrant growth signalling in Niemann–Pick type C. Nat. Cell Biol. *21*, 1206–1218.
38. Abu-Remaileh, M., Wyant, G.A., Kim, C., Laqtom, N.N., Abbasi, M., Chan, S.H., Freinkman, E., and Sabatini, D.M. (2017). Lysosomal metabolomics reveals V-ATPase and mTOR-dependent regulation of amino acid efflux from lysosomes. Science *358*, 807–813.
39. Shin, S., Zhou, H., He, C., Wei, Y., Wang, Y., Shingu, T., Zeng, A., Wang, S., Zhou, X., Li, H., et al. (2021). Qki activates Srebp2-mediated cholesterol biosynthesis for maintenance of eye lens transparency. Nat. Commun. *12*, 3005.
40. Zhou, X., Shin, S., He, C., Zhang, Q., Rasband, M.N., Ren, J., Dai, C., Zorrilla-Veloz, R.I., Shingu, T., Yuan, L., et al. (2021). Qki regulates myelinogenesis through Srebp2-dependent cholesterol biosynthesis. Elife *10*, e60467.
41. Lu, F., Liang, Q., Abi-Mosleh, L., Das, A., De Brabander, J.K., Goldstein, J.L., and Brown, M.S. (2015). Identification of NPC1 as the target of U18666A, an inhibitor of lysosomal cholesterol export and Ebola infection. Elife *4*, e12177.
42. Ilnytska, O., Lai, K., Gorshkov, K., Schultz, M.L., Tran, B.N., Jeziorek, M., Kunkel, T.J., Azaria, R.D., McLoughlin, H.S., Waghalter, M., et al. (2021). Enrichment of NPC1-deficient cells with the lipid LBPA stimulates autophagy, improves lysosomal function, and reduces cholesterol storage. J. Biol. Chem. *297*, 100813.
43. Hailfinger, S., Lenz, G., Ngo, V., Posvitz-Fejfar, A., Rebeaud, F., Guzzardi, M., Penas, E.-M.M., Dierlamm, J., Chan, W.C., Staudt, L.M., and Thome, M. (2009). Essential role of MALT1 protease activity in activated B cell-like diffuse large B-cell lymphoma. Proc. Natl. Acad. Sci. USA *106*, 19946–19951.
44. Ferch, U., Kloo, B., Gewies, A., Pfänder, V., Düwel, M., Peschel, C., Krappmann, D., and Ruland, J. (2009). Inhibition of MALT1 protease activity is selectively toxic for activated B cell-like diffuse large B cell lymphoma cells. J. Exp. Med. *206*, 2313–2320.
45. März, P., Otten, U., and Miserez, A.R. (2007). Statins induce differentiation and cell death in neurons and astroglia. Glia *55*, 1–12.
46. Shammas, H., Kuech, E.-M., Rizk, S., Das, A.M., and Naim, H.Y. (2019). Different Niemann-Pick C1 Genotypes Generate Protein Phenotypes

that Vary in their Intracellular Processing, Trafficking and Localization. Sci. Rep. *9*, 5292.

47. Sarkar, S., Carroll, B., Buganim, Y., Maetzel, D., Ng, A.H.M., Cassady, J.P., Cohen, M.A., Chakraborty, S., Wang, H., Spooner, E., et al. (2013). Impaired Autophagy in the Lipid-Storage Disorder Niemann-Pick Type C1 Disease. Cell Rep. *5*, 1302–1315.
48. Moreau, D., Vacca, F., Vossio, S., Scott, C., Colaco, A., Paz Montoya, J., Ferguson, C., Damme, M., Moniatte, M., Parton, R.G., et al. (2019). Drug-induced increase in lysobisphosphatidic acid reduces the cholesterol overload in Niemann–Pick type C cells and mice. EMBO Rep. *20*, e47055.
49. Harford-Wright, E., Andre-Gregoire, G., Jacobs, K.A., Treps, L., Le Gonidec, S., Leclair, H.M., Gonzalez-Diest, S., Roux, Q., Guillonneau, F., Loussouarn, D., et al. (2017). Pharmacological targeting of apelin impairs glioblastoma growth. Brain *140*, 2939–2954.
50. Le Guelte, A., Galan-Moya, E.-M., Dwyer, J., Treps, L., Kettler, G., Hebda, J.K., Dubois, S., Auffray, C., Chneiweiss, H., Bidere, N., and Gavard, J. (2012). Semaphorin 3A elevates endothelial cell permeability through PP2A inactivation. J. Cell Sci. *125*, 4137–4146.
51. André-Grégoire, G., Maghe, C., Douanne, T., Rosińska, S., Spinelli, F., Thys, A., Trillet, K., Jacobs, K.A., Ballu, C., Dupont, A., et al. (2022). Inhibition of the pseudokinase MLKL alters extracellular vesicle release and reduces tumor growth in glioblastoma. iScience *25*, 105118.
52. Trillet, K., Jacobs, K.A., André-Grégoire, G., Thys, A., Maghe, C., Cruard, J., Minvielle, S., Diest, S.G., Montagnac, G., Bidère, N., and Gavard, J. (2021). The glycoprotein GP130 governs the surface presentation of the G protein–coupled receptor APLNR. J. Cell Biol. *220*, e202004114.
53. Bowman, R.L., Wang, Q., Carro, A., Verhaak, R.G.W., and Squatrito, M. (2017). GlioVis data portal for visualization and analysis of brain tumor expression datasets. Neuro Oncol. *19*, 139–141.
54. Lachuer, H., Le, L., Lévêque-Fort, S., Goud, B., and Schauer, K. (2023). Spatial organization of lysosomal exocytosis relies on membrane tension gradients. Proc. Natl. Acad. Sci. *120*, e2207425120.
55. Kulak, N.A., Pichler, G., Paron, I., Nagaraj, N., and Mann, M. (2014). Minimal, encapsulated proteomic-sample processing applied to copy-number estimation in eukaryotic cells. Nat. Methods *11*, 319–324.
56. Tyanova, S., Temu, T., Carlson, A., Sinitcyn, P., Mann, M., and Cox, J. (2015). Visualization of LC-MS/MS proteomics data in MaxQuant. Proteomics *15*, 1453–1456.
57. Raudvere, U., Kolberg, L., Kuzmin, I., Arak, T., Adler, P., Peterson, H., and Vilo, J. (2019). g:Profiler: a web server for functional enrichment analysis and conversions of gene lists (2019 update). Nucleic Acids Res. *47*, W191–W198.

STAR★METHODS

KEY RESOURCES TABLE

REAGENT or RESOURCE	SOURCE	IDENTIFIER
Antibodies		
CALRETICULIN	Cell Signaling Technology	Cat#12238; RRID:AB_2688013
CATHEPSIN D	BD Biosciences	Cat#610800; RRID:AB_398119
EEA1	BD Biosciences	Cat#610456; RRID:AB_397829
FLAG	Cell Signaling Technology	Cat#F1804; RRID:AB_262044
GAPDH	Santa Cruz Biotechnology	Cat#sc-32233; RRID:AB_627679
GM130	Abcam	Cat#ab52649; RRID:AB_880266
HA	Merck Millipore	Cat#H3663; RRID:AB_262051
HA	Cell Signaling Technology	Cat#3724; RRID:AB_1549585
HOIL1	Santa Cruz Biotechnology	Cat#sc-393754
LAMP2	Santa Cruz Biotechnology	Cat#sc-18822; RRID:AB_626858
LBPA	Merck Millipore	Cat#MABT837
LC3B	Cell Signaling Technology	Cat#3868; RRID:AB_2137707
LDLR	Proteintech	Cat#10785-1-AP; RRID:AB_2281164
NPC1	Abcam	Cat#ab134113; RRID:AB_2734695
NPC2	ABclonal	Cat#A5413; RRID:AB_2766221
P62	Cell Signaling Technology	Cat#88588; RRID:AB_2800125
QKI	Santa Cruz Biotechnology	Cat#sc-517305; RRID:AB_2941818
SREBP2	R&D Systems	Cat#MAB7119
SREBP2	Cayman Chemical	Cat#10007663; RRID:AB_2615896
VDAC	Cell Signaling Technology	Cat#4661; RRID:AB_10557420
α-TUBULIN	Proteintech	Cat#66031-1-Ig; RRID:AB_11042766
α-TUBULIN	Santa Cruz Biotechnology	Cat#sc-8035; RRID:AB_628408
Goat Anti-Mouse Ig, Human ads-HRP	Southern Biotech	Cat#1010-05
Goat Anti-Mouse IgG1, Human ads-HRP	Southern Biotech	Cat#1070-05
Goat Anti-Mouse IgG2a, Human ads-HRP	Southern Biotech	Cat#1080-05
Goat Anti-Mouse IgG2b, Human ads-HRP	Southern Biotech	Cat#1090-05
Goat Anti-Rabbit IgG(H + L), Mouse/Human ads-HRP	Southern Biotech	Cat#4050-05
Goat anti-Mouse IgG1 Cross-Adsorbed Secondary Antibody, Alexa Fluor 546	Life Technologies	Cat#A-21123
Goat anti-Rabbit IgG (H + L) Highly Cross-Adsorbed Secondary Antibody, Alexa Fluor 546	Life Technologies	Cat#A-11035
Goat anti-Mouse IgG1 Cross-Adsorbed Secondary Antibody, Alexa Fluor 488	Life Technologies	Cat#A-21121
Goat anti-Rabbit IgG (H + L) Highly Cross-Adsorbed Secondary Antibody, Alexa Fluor 488	Life Technologies	Cat#A-11034
Bacterial and virus strains		
One Shot Stbl3 Chemically Competent E. coli	Life Technologies	Cat#C7373-03
Biological samples		
Patient-derived glioblastoma stem-like cells GSC#1, GSC#4, GSC#6, GSC#9	Harford-Wright E. et al. (2017)	N/A
GSC#9 3xHA	This paper	N/A
GSC#9 2xFLAG	This paper	N/A
Luciferase-GFP-expressing GSC#9	André-Grégoire G. et al. (2022)	N/A

(*Continued on next page*)

Continued

REAGENT or RESOURCE	SOURCE	IDENTIFIER
Chemicals, peptides, and recombinant proteins		
Mepazine	ChemBridge	Cat#5216177; CAS: 738596-90-2
MLT-748	Selleck Chemicals	Cat#S8898; CAS: 1832578-30-9
U18666A	Selleck Chemicals	Cat#S9669; CAS: 3039-71-2
Cerivastatin	Merck Millipore	Cat#SML0005; CAS: 143201-11-0
LLOMe	Merck Millipore	Cat#L7393; CAS: 16689-14-8
Clemastine	Selleck Chemicals	Cat#S1847; CAS: 14976-57-9
Raptinal	Merck Millipore	Cat#SML-1745; CAS: 1176-09-6
Cholesterol	Merck Millipore	Cat#C3045; CAS: 57-88-5
Methyl-β-cyclodextrin (MβCD)	Merck Millipore	Cat#C4555; CAS: 128446-36-6
Ponceau S Solution	Santa Cruz Biotechnology	Cat#sc-301558; CAS: 6226-79-5
Paraformaldehyde (PFA)	Electron Microscopy Sciences	Cat#15710; CAS: 30525-89-4
Triton X-100	Merck Millipore	Cat#T9284; CAS: 9036-19-5
Bovine Serum Albumin (BSA)	Merck Millipore	Cat#A2153; CAS: 9048-46-8
DAPI Solution	Life Technologies	Cat#62248; CAS: 28718-90-3
Glycin	Eurobio Scientific	Cat#GEPGLY00-66; CAS: 56-40-6
Filipin Complex from *Streptomyces filipinensis*	Merck Millipore	Cat#F9765; CAS: 11078-21-0
Fibronectin	Merck Millipore	Cat#F1056; CAS: 86088-83-7
Matrigel	Corning	Cat#356237
Critical commercial assays		
BC assay: protein assay kit	Interchim	Cat#FT-40840A
CellTiter-Glo 2.0 Cell Viability Assay	Promega	Cat#G9243
Duolink *In Situ* Detection Reagents Far Red	Merck Millipore	Cat#DUO92013
Duolink *In Situ* PLA Probe Anti-Mouse PLUS	Merck Millipore	Cat#DUO92001
Duolink *In Situ* PLA Probe Anti-Rabbit MINUS	Merck Millipore	Cat#DUO92005
Dual-Luciferase Reporter Assay System	Promega	Cat#E1910
Cholesterol/Cholesterol Ester-Glo Assay	Promega	Cat#J3190
Blood cholesterol measurement kit	Sobioda	Cat#W1306139
Pierce^{TM} Magnetic ChIP Kit	Life Technologies	Cat#26157
Propidium iodide	Life Technologies	Cat#V13245
Deposited data		
Label-free quantification proteomic analysis of total cell lysates from vehicle versus mepazine-treated GSC#9	This paper	PXD040862
Label-free quantification proteomic analysis of immunopurified lysosomes (LysoIP) from vehicle versus mepazine-treated GSC#9	This paper	PXD040855
RNAseq analysis of vehicle versus mepazine-treated GSC#9	Jacobs et al. (2020)[5]	GSE139018
Experimental models: Cell lines		
HEK293T embryonic kidney cells	ATCC	Cat#CRL-3216; RRID:CVCL_0063
Jurkat T-cells E6-1	ATCC	Cat#TIB-152; RRID:CVCL_0367
BJAB Burkitt lymphoma cells	DSMZ	Cat#ACC 757; RRID:CVCL_5711
OCI-LY3 B-lymphoma cells	DSMZ	Cat#ACC 761
hCMEC/D3 brain endothelial cells	Gift from Couraud P.O.	N/A
SVG p12 astrocytes	ATCC	Cat#CRL-8621; RRID:CVCL_3797
Experimental models: Organisms/strains		
Mouse: BALB/CAnN.Cg-Foxn1 nu/nu	Charles River	N/A

(*Continued on next page*)

Continued

REAGENT or RESOURCE	SOURCE	IDENTIFIER
Oligonucleotides		
Stealth non-silencing low-GC RNA duplexes CGACAAUUGUGAGGUCUAAACUAUU	Life Technologies	Cat#12935111
siRNA targeting human MALT1 (si.2MALT1) CAGCAUUCUGGAUUGGCAAAUGGAA	This paper	N/A
siRNA targeting human MALT1 (si.3MALT1) CCUGUGAAAUAGUACUGCACUUACA	Life Technologies	Cat#10620312
siRNA targeting human NPC1 (siNPC1) ACCAATTGTGATAGCAATATT	This paper	N/A
siRNA targeting human NPC2 (siNPC2) GGAUGGAGUUAUAAAGGAA	This paper	N/A
siRNA targeting human SREBP2 (siSREBP2) GCGCUCUCAUUUUACCAAATT	This paper	N/A
siRNA targeting human QKI (siQKI) CCTTGAGTATCCTATTGAACCTAGT	Life Technologies	Cat#1299001
Primers for qPCR and ChIP-qPCR, see Table S4	This paper	N/A
Recombinant DNA		
pLJC5-Tmem192-3xHA	Addgene	Cat#102930; RRID:Addgene_102930
pLJC5-Tmem192-2xFLAG	Addgene	Cat#102929; RRID:Addgene_102929
pSynSRE-T-Luc	Addgene	Cat#60444; RRID:Addgene_60444
pSynSRE-Mut-T-Luc	Addgene	Cat#60490; RRID:Addgene_60490
pRL-TK-Renilla-Luc	Promega	Cat#E2241
psPAX2	Addgene	Cat#12260
pCMV-VSV-G	Addgene	Cat#8454
Mixture of pLNT-LucF/pFG12-eGFP	André-Grégoire G. et al. (2022)	N/A
Software and algorithms		
Gliovis Platform	Bowman R. et al. (2017)	Version: 0.20
ImageJ/FIJI	NIH	Version: 2.3.0/1.53q
g:Profiler	Raudvere, U. et al. (2019)	Version: e107_e.g.,54_p17_bf42210
Panther Classification System	Thomas P.D. et al. (2022)	Version: 17.0
Prism 9.3.0.463	GraphPad	Serial number: GPS-2575813-L###-####
FlowJo X	BD Biosciences	Version: 10.0.7r2
NIS-Elements	Nikon	Version: 5.30.03
Other		
N-2 Supplement	LifeTechnologies	Cat#17502048
G-5 Supplement	LifeTechnologies	Cat# 17503012
B-27 Supplement	LifeTechnologies	Cat#17504044
GeneJuice Transfection Reagent	Merck Millipore	Cat#70967
Lipofectamine RNAiMAX Transfection Reagent	LifeTechnologies	Cat#13778150
HALT Protease Inhibitor Cocktail	LifeTechnologies	Cat#78429
Substrat HRP Immobilon Western	Merck Millipore	Cat# WBKLS0500
FUSION FX Imaging System	Vilber	Cat#FUSION-FX7-826.WL/SuperBright
Protran Nitrocellulose Western Blotting Membranes	Amersham	Cat#GE10600002
Dil Labeled Native LDL	Kalen Biomedical, LLC	Cat#NC9839048
ProLong Gold Antifade Mountant	Life Technologies	Cat#P36934
NucleoSpin RNA, Mini Kit for RNA Purification	Macherey-Nagel	Cat#740955
Maxima First Strand cDNA Synthesis Kit for RT-qPCR	Life Technologies	Cat#K1642
PerfeCTa SYBR Green FastMix Low ROX	QuantaBio	Cat#95074-05K
FLUOstar Optima Plate Reader	BMG Labtech	Serial number: 413-3408

(*Continued on next page*)

Continued

REAGENT or RESOURCE	SOURCE	IDENTIFIER
Pierce Anti-HA Magnetic Beads	Life Technologies	Cat#88837
LysoTracker^{TM} Red DND-99	Life Technologies	Cat#L7528
Charcoal Stipped Fetal Bovine Serum, Delipidated	Life Technologies	Cat#A3382101
Polybrene	Santa Cruz Biotechnology	Cat#sc-134220

RESOURCE AVAILABILITY

Lead contact

Further information and requests for resources and reagents should be directed to and will be fulfilled by the lead contact, Julie Gavard (julie.gavard@inserm.fr).

Materials availability

This study did not generate new unique reagents.

Data and code availability

This paper analyzed existing, publicly available RNAseq data deposited in Gene Expression Omnibus (GEO) under the accession numbers GEO: GSE139018.

Raw and processed proteomic data have been deposited at ProteomeXchange with identifiers PXD040862 for whole cell lysate analysis, and PXD040855 for immunopurified lysosomes-targeted proteomic, and are publicly available as of the date of publication.

This paper does not report original code.

Any additional information required to reanalyze the data reported in this paper is available from the lead contact upon request.

EXPERIMENTAL MODEL AND STUDY PARTICIPANT DETAILS

Animals

Animal experiments were approved by the French Government (Ministry of Higher Education and Research, APAFIS#24400–2020022713064016 v2) and conducted in agreement with the European Convention for the Protection of Vertebrate Animals used for Experimental and other Scientific Purposes (ETS 123). Animals had continuous access to food and water, in a specific pathogen-free (SPF) environment with regulated temperature and hygrometry, following a 12h day-night cycle. Xenografts were conducted on six-to-seven-weeks-old female Balb/c Nude mice (BALB/CAnN.Cg-Foxn1 nu/nu, Janvier Labs).

Cell culture

All cells were cultured according to the French Ministry of Higher Education and Research rules under the #DUO10524 authorization. GB patient-derived stem-like cells (GSCs) were dissociated from primary glioblastoma tissue (MACS Dissociator, Miltenyi). All subjects have given their informed consent. This study was approved by the institutional review boards of Sainte-Anne Hospital, Paris, France, and Laennec Hospital, Nantes, France, and performed in accordance with the Declaration of Helsinki Protocol. They were characterized for their self-renewal capabilities, cell surface antigens, expression of stemness markers, their ability to differentiate, and to initiate tumor formation.[49] GSC#1 (mesenchymal, 68-year-old male), GSC#4 (mesenchymal, 76-year-old female), GSC#6 (mesenchymal, 68-year-old male), and GSC#9 (classical, 68-year-old female) were routinely cultured in sphere-forming conditions in serum-free NS34 medium (DMEM-F12, Glutamax, and antibiotics, further supplemented with N2, G5, and B27). HEK293T human embryonic kidney cells, Jurkat E6.1 T lymphocyte cells, SVG-p12 human astrocyte, OCI-Ly3 B-lymphoma cells and BJAB Burkitt lymphoma cells were cultured as per the manufacturer's instructions. Human brain endothelial cells (hCMEC/D3) were a gift from P.O. Couraud (Institut Cochin, Paris, France) and cultured accordingly.[50]

METHOD DETAILS

Mice xenograft models

Six-to-seven-weeks-old female Balb/c nude mice (Janvier Labs) were subcutaneously injected in each flank with GFP-Luciferase-expressing $0.5.10^5$ GSC#9.[51] Tumorspheres were dissociated prior to injection to ensure implantation of a single cell suspension in PBS:matrigel (1:1).

Ten days after grafts, mice were treated intraperitoneally 5 times per week with vehicle (10% DMSO in PBS), MLT-748 (4 mg/kg), or U18666A (4 mg/kg), until a critical point was reached (tumor volume >1000 mm^3). Tumor size was measured twice a week with calipers and tumor volume calculated using the following equation $(\text{width}^2 \times \text{length})/2$. At euthanasia, tumors were dissected and fixed in PFA. Total blood was collected by intracardiac puncture on EDTA tubes and centrifugated (1000xg, 15min, 4°C) before freezing at −80°C. Blood cholesterol measurement was performed following company instruction (Sobioda).

siRNA transfection

RNA duplexes targeting the respective human genes were transfected using RNAiMAX Lipofectamine. Stealth non-silencing Low-GC RNA duplexes (si^{ctl}) were used as non-silencing control.

Plasmid transfection and lentiviral transduction

SRE-T-Luc, SRE-Mut-T-Luc, and renilla plasmid transfection was performed using the GeneJuice transfection reagent following the manufacturer's instructions. For stable expression of TMEM192-3xHA and TMEM192-2xFLAG, lentiviral particles were produced in HEK-293T cells, according to established procedures.[52] Briefly, cells were transfected with pPAX2 and pVSVg and supernatants were collected after 2 days. Particles were applied on GSC#9 during a 1,000g centrifugation for 90 min in the presence of 8 μg/mL polybrene. For selection, cells were cultured with 1 μg/mL puromycin.

TCGA analysis

The Cancer Genome Atlas (TCGA) was interrogated using the Gliovis Platform (http://gliovis.bioinfo.cnio.es).[53] RNAseq (155 patients) and Agilent 4502A (488 patients) databases were used to investigate data related to SREBP1/2 and NPC1/2, respectively (RNA expression, probability of survival, and number at risks). All subtypes of Grade IV, Glioblastoma were included. Low/High expression groups were set at median expression for each individual gene. They were further classified into 3 groups of High/High, Mixed, and Low/Low NPC1 and NPC2 expression. Again, RNA expression, probability of survival, and number at risks were analyzed.

Cholesterol/MβCD complexes preparation

Cholesterol was dissolved to a final concentration of 5 mM in a solution of 0.1% MβCD prepared in sterile H_2O. The solution was vigorously vortexed, heated at 37°C for 2h, and stored at 4°C.

Cell lysis and western-blots

Cells were harvested on ice, washed in cold PBS, pelleted (500xg, 3 min, 4°C) and lysed in RIPA buffer (25 mM Tris-HCl pH 7.4, 150 mM NaCl, 0.1% SDS, 0.5% Na-Deoxycholate, 1% NP-40, 1 mM EDTA) supplemented with Halt protease inhibitor cocktail for 30 min on ice. Lysates were cleared by centrifugation (10,000xg, 10 min, 4°C) to pellet insoluble debris and nuclei. Protein concentrations in supernatants were determined using a micro-BCA assay kit. An equal amount of proteins (10 μg) was resolved by SDS-PAGE and transferred onto nitrocellulose membranes. Proteins were fixed to the membranes using a Ponceau S solution, and nonspecific protein binding sites were saturated with 5% milk in PBS-Tween 0.05%. Primary (1/1,000 dilution except LAMP2 at 1/5,000, GAPDH at 1/20,000) and secondary (1/5,000 dilution) antibodies were incubated with membranes in a similar blocking solution. Revelation was performed using Immobilon western chemiluminescent HRP substrate and the Fusion imaging system.

Cellular fractionation

15.10^6 GSC#9 were treated as indicated, washed in PBS, and resuspended in a hypotonic buffer (20 mM HEPES, 1.5 mM $MgCl_2$, 60 mM KCl, in H_2O) containing anti-proteases. Some cells were collected before lysis for whole cell lysate input. Cells were lysed with 15 strokes of a 29-gauge syringe at 4°C. Nuclei were pelleted with a 1,000xg centrifugation for 5 min at 4°C and discarded. The supernatant was centrifuged at 100,000xg for 1h at 4°C (S100). The pellet was washed once with hypotonic buffer at 100,000xg for 1h at 4°C and lysed with RIPA lysis buffer (P100). S100 and P100 fractions were then processed for Western blot analysis.

Cell viability and cell death assays

Cell viability was measured using CellTiter-Glo luminescent cell viability assay following the manufacturer's protocol. Experiments were performed in 96-well plates in 100 μL final volume of media. Briefly, GSCs were seeded at 10,000 cells per well in triplicate for 2 days with the indicated drugs and vehicle. Alternatively, GSCs were seeded at 8,000 cells per well in triplicate for each condition and further challenged with siRNA transfection. Viability was read after 3 more days. Experiments were harvested by the addition of 100 μL of the CellTiter-Glo reagent and luminescence was read using a FLUOstar Optima plate reader. For propidium iodide (PI) staining, cells were treated as mentioned and PI (100 μg/mL) was added for 10 min at room temperature according to the manufacturer's protocol. Flow cytometry analyses were performed on FACSCanto II (Cytocell core facility, UMS Biocore, Inserm US16, UAR CNRS 3556, Nantes Université, Nantes, France). All data were analyzed on FlowJo. For cell viability assays using HEK293T human embryonic kidney cells, Jurkat E6.1 T lymphocyte cells, SVG-p12 human astrocytes, hCMEC/D3 human brain endothelial cells, OCI-Ly3 B-lymphoma cells and BJAB Burkitt lymphoma cells, cells were cultured in their routine culture medium containing FBS and processed as GSCs. For each cell line, data were normalized to their respective control DMSO treatment.

Immunofluorescence staining

3.10^5 cells were seeded onto glass slides and fixed for 12 min at room temperature with a solution of 4% paraformaldehyde (PFA) diluted in PBS. Cells were permeabilized using a solution of Triton X-100 (0.2%) diluted in PBS, for 5 min at room temperature.

Blocking solution (4% BSA in PBS) was added for 30 min prior to incubation 1h at room temperature with primary antibodies (1/200 dilution in the blocking solution). Secondary antibodies (1/400 dilution in the blocking solution) were applied, and samples were further processed for confocal analysis. For LysoTracker staining, cells were incubated with 100 nM of the probe for 30 min at 37°C before PFA fixation (4%, 12min, room temperature), and further processed for confocal analysis. For dil-LDL uptake, 3.10^5 cells were treated as indicated (16h for drug treatments, 3 days for siRNA transfection), followed by incubation with dil-LDL (5 μg/mL) for 2h at 37°C. Cells were then seeded onto glass slides and fixed for 12 min at room temperature with 4% PFA and further processed for confocal analysis.

Micropatterning

Ring-shaped micropatterned coverslips were prepared using the photolithography method and provided by K. Schauer (Institut Gustave Roussy, Villejuif, France).[54] For use with GSCs, micropatterned were first coated with 50 μg/mL of fibronectin for 1h at room temperature. Then, 60,000 cells were seeded in NS34 in the presence of 10% FBS. Following 1 h of incubation at 37°C, coverslips were washed 5 times with culture media to remove non-attached cells. Cells were then incubated overnight at 37°C before fixation with 4% PFA. Immunofluorescent staining was performed as described and processed for confocal analysis.

Proximity ligation assay (PLA)

PLA was performed using the Duolink *in situ* detection reagents far-red kit, PLA-probe anti-mouse PLUS, and PLA-probe anti-rabbit MINUS, according to the manufacturer's protocol. Briefly, GSCs were treated as indicated (3 days siRNA transfection or 6h drug treatment) and seeded onto glass slides before PFA fixation and Triton X-100 permeabilization. Primary antibodies (anti-HA, 1/1,000 and anti-NPC1, 1/200) were incubated at 4°C for 16h in a humid chamber before processing according to the manufacturer's protocol. Samples were processed for confocal analysis.

Confocal analysis

Except when mentioned, nuclei were stained with DAPI (1/5,000) and slides were mounted with prolong gold anti-fade mounting medium before imaging. Images were acquired on confocal Nikon A1 Rsi, using a 60x oil-immersion lens (IBISA MicroPICell facility, UMS Biocore, Inserm US16, UAR CNRS 3556, Nantes Université, Nantes, France). Unless otherwise specified in figures legends, images were visualized as single confocal plans. All images were analyzed and quantified using the ImageJ software.

Filipin-III staining for imaging and flow cytometry

Cells were seeded onto glass slides and fixed for 12 min at room temperature with a solution of 4% PFA diluted in PBS. PFA was quenched for 10 min at room temperature using a glycine/PBS solution (1.5 mg/mL). The filipin-III stock solution (25 mg/mL in DMSO) was diluted to 0.5 mg/mL in a 4% bovine serum albumin (BSA) solution and added to the cells for 2h at room temperature. Finally, cells were mounted with prolong gold anti-fade mounting medium. Alternatively, cells were incubated with the filipin-III/BSA solution for 30 min prior to antibody incubation. Primary antibodies were diluted in the filipin-III/BSA solution and added for 1h, followed by 30 min with secondary antibodies also diluted in the solution of filipin-III/BSA. No DAPI counterstaining was performed because the excitation wavelength is the same as filipin-III. Slides were imaged on a Zeiss AXIO Observer.Z1. For enhanced resolution, images were further deconvoluted using the Nikon Imaging System (NIS-Elements) software. For FACS analysis, GSCs were similarly processed in 96-V-well plates and using a filipin-III concentration of 0.125 mg/mL diluted in PBS. Fluorescence intensity was measured using the UV 379/28 laser (BD FACSymphony A5, Cytocell core facility, UMS Biocore, Inserm US16, UAR CNRS 3556, Nantes Université, Nantes, France). All data were analyzed with FlowJo.

qPCR analysis

RNA was extracted from 1.10^6 GSCs using the NucleoSpin RNA Plus purification kit. Equal amounts of RNA were reverse-transcribed using the Maxima First Strand cDNA Synthesis kit, and 30 ng of the resulting cDNA was amplified by qPCR using PerfeCTa SYBR Green SuperMix Low ROX. Data were analyzed using the 2-ΔΔCt methods and normalized by the housekeeping genes ACTB and HPRT1. All primers used are listed in Table S4.

ChIP-qPCR

The ChIPq-PCR assay was performed using the Pierce Magnetic ChIP Kit according to the manufacturer's protocol. Briefly, GSC#9 cells were treated with vehicle or MPZ (20 μM) for 6h and samples were crosslinked in a PBS/PFA solution (1%) for 10 min. Glycine was added to quench PFA before PBS washes. Cell pellets were lysed with 100 μL of IP buffer containing anti-proteases before MNase digestion of DNA for 15 min at 37°C. Fragmented DNA was released from cells by sonication using a Bioruptor plus (Diagenode) device, and parameters were as follows: HIGH setting, 6 cycles of 30 s ON/30 s OFF. Supernantants containing fragmented DNA were collected after a 5 min, 9,000xg centrifugation. 10 μL of the DNA-containing supernatant was saved as 10% input control. The remaining 90 μL were incubated with primary antibodies solutions (anti-RNA Pol II, Normal Rabbit IgG, anti-SREBP2, 5 mg/mL) for 16 h at 4°C with rotation. 20 μL of magnetic beads were added to each IP reaction and incubated for 2h at 4°C with rotation. A magnetic stand was used to wash the beads. Immunopurified DNA fragments were eluted at 65°C for 40 min and by vortexing every 10 min. Proteins from IP samples and inputs were removed by incubation with proteinase K for 1h30 at 65°C. DNA was recovered using the columns and buffers furnished in the kit. qPCR was performed according to the manufacturer's recommendations. All primers used are listed in Table S4.

RNAseq analysis

5.10^6 GSC#9 cells were treated for 4h with a vehicle (DMSO) or MPZ (20 μM) and snap-frozen on dry ice. Samples and data were processed at Active Motif (Carlsbad, California, USA). Briefly, 2 μg of total RNA was isolated using the Qiagen RNeasy Mini Kit and further processed in Illumina's TruSeq Stranded mRNA Library kit. Libraries are sequenced on Illumina NextSeq 500 as paired-end 42-nt reads. Sequence reads are analyzed with the STAR alignment—DESeq2 software pipeline.[5] The RNAseq data have been deposited to the Gene Expression Omnibus (GEO) platform and are available with the dataset identifier GSE139018.

Luciferase SREBP2 reporter assay

2.10^6 cells were transfected with 2 μg of either pSynSRE-T-Luc (SRE wild-type) or pSynSRE-Mut-T-Luc (SRE-mut), to which SREBP2 cannot bind, in combination with 0.1 μg pRL-TK-Renilla using the GeneJuice transfection reagent. After 24h, cells were seeded in a 96-well plate in triplicate per condition and cultured for further 16h in the presence of the indicated drugs. At the end of the experiment, cells were pelleted and lysed with 30 μL of lysis buffer. 20 μL of the lysate was revealed using the Dual-Glo luciferase assay system following the manufacturer's protocol. Luminescence was measured using a FLUOstar Optima plate reader. Luminescence values were calculated as the ratio SRE_{WT}/SRE_{Mut}, and further normalized to Renilla intensities.

Cholesterol dosage

Cellular cholesterol was measured using the Cholesterol/Cholesterol Ester-Glo Assay Kit following manufacturer's instructions. Briefly, 1.10^5 GSCs were lysed for 30 min at 37°C. A volume of 25 μL of the lysate was used for cholesterol quantification. Cholesterol level was determined by reading luminescence after 1h incubation with cholesterol reductase and cholesterol esterase reagents at room temperature. Cholesterol concentration was extrapolated from a standard curve prepared for each experiment and normalized to protein concentration.

Lysosome immunoprecipitation (LysoIP)

15.10^6 GSCs expressing TMEM192-3xHA were used per condition. TMEM192-2xFLAG expressing cells were used as a control. Each step was conducted at 4°C. After the indicated treatments, cells were washed in cold PBS and centrifuged at 1,000xg for 2 min. Pelleted cells were resuspended in 500 μL cold PBS + anti-proteases and 100 μL were saved for whole cell lysate control. The remaining 400 μL were mechanically lysed with 10 strokes of a 29-gauge syringe and centrifuged at 1,000xg for 2 min. Supernatants containing organelles were incubated with 75 μL of Pierce anti-HA magnetic beads for 15 min under rotation. Beads were then washed 3 times with cold PBS + anti-proteases. For further analysis, beads were eluted twice with 50 μL of elution buffer (50 mM Tris/HCl pH 8.5 with 2% SDS) and boiled at 95°C for 5 min. Eluates were further processed for Western blot and proteomic analyses. Alternatively, samples were stored at −80°C.

Label-free quantification (LFQ) proteomic processing and analysis of whole cell lysates

For sample preparation, pelleted cells were solubilized in lysis buffer (2% SDS, 200 mM TEAB, pH 8.5) and heated for 5 min at 95°C. The protein concentration of the supernatants was estimated with a BCA assay. Proteins were then reduced and alkylated with 10 mM TCEP and 50 mM chloroacetamide. Bottom-up experiments' tryptic peptides were obtained by S-Trap Micro Spin Column according to the manufacturer's protocol (Protifi, NY, USA). Briefly, 30 μg of proteins were digested during 14 h at 37°C with 1 μg Trypsin sequencing grade (Promega). The S-Trap Micro Spin Column was used according to the manufacturer's protocol. After speed-vacuum drying, eluted peptides were solubilized in 2% trifluoroacetic acid (TFA) and fractionated by strong cationic exchange (SCX) Stage-Tips.[55]

Liquid Chromatography-coupled Mass spectrometry analysis (LC-MS) analyses were performed on a Dionex U3000 RSLC nano-LC- system (Thermo Fisher scientific, Les Ulis, France) coupled to a TIMS-TOF Pro mass spectrometer (Bruker Daltonik GmbH, Bremen, Germany). After drying, peptides from SCX Stage-Tip, the 5 fractions were solubilized in 10 μL of 0.1% TFA containing 10% acetonitrile (ACN). 1 μL was loaded, concentrated, and washed for 3 min on a C_{18} reverse phase precolumn (3 μm particle size, 100 Å pore size, 75 μm inner diameter, 2 cm length, from Thermo Fisher Scientific). Peptides were separated on an Aurora C_{18} reverse phase resin (1.6 μm particle size, 100Å pore size, 75 μm inner diameter, 25 cm length mounted to the Captive nanoSpray Ionisation module, IonOpticks, Middle Camberwell Australia) with a 120-min overall run time with a gradient ranging from 99% of solvent A containing 0.1% formic acid in milliQ-grade H_2O to 40% of solvent B containing 80% acetonitrile, 0.085% formic acid in mQH_2O. The mass spectrometer acquired data throughout the elution process and operated in DDA PASEF mode with a 1.1 s/cycle, with Timed Ion Mobility Spectrometry (TIMS) mode enabled and a data-dependent scheme with full MS scans in Parallel Accumulation and Serial Fragmentation (PASEF) mode. This enabled a recurrent loop analysis of a maximum of the 120 most intense nLC-eluting peptides which were CID-fragmented between each full scan every 1.1sec. Ion accumulation and ramp time in the dual TIMS analyzer were set to 166 msec each and the ion mobility range was set from 1/K0 = 0.6 Vs. cm^{-2} to 1.6 Vs. cm^{-2}. Precursor ions for MS/MS analysis were isolated in positive mode with the PASEF mode set to « on » in the 100–1.700 m/z range by synchronizing quadrupole switching events with the precursor elution profile from the TIMS device. Singly charged precursor ions were excluded from the TIMS stage by tuning the TIMS using the otof control software, (Bruker Daltonik GmbH). Precursors for MS/MS were picked from an intensity threshold of 1000 arbitrary units (a.u.) and resequenced until reaching a ‘target value’ of 20.000 a.u. taking into account a dynamic exclusion of 0.40 s elution gap.

Regarding protein quantification and comparison, mass spectrometry data were analyzed using Maxquant version 1.6.6.0.[56] The database used was a *Human* sequence from the Uniprot databases (release March 2020). The enzyme specificity was that for trypsin. The cleavage specificity was trypsin’s with maximum 2 missed cleavages. Carbamidomethylation of cysteines was set as constant modification, whereas acetylation of the protein N terminus and oxidation of methionines were set as variable modifications. The false discovery rate was kept below 1% on both peptides and proteins. Label-free protein quantification (LFQ) was performed using both unique and razor peptides. At least two such peptides were required for LFQ. The “match between runs” (MBR) option was allowed with a match time window of 0.7min and an alignment time window of 20min. For differential analysis, LFQ results from MaxQuant, were imported into Perseus software version 1.6.14.0 (Max-Planck Institute of Biochemistry). Reverse and contaminant proteins were excluded from the bioinformatic analysis. LFQ data were transformed into $\log_2$. A t test (p value<0,05) was carried out on proteins and proteins with at least 3 valid values in at least one group. Moreover, PCA (principal component analysis) was performed on all proteins with imputation.

Label-free quantification (LFQ) proteomic processing and analysis of LysoIP

For sample preparation, IP samples were solubilized in lysis buffer (2% SDS, 200 mM Tris-HCl, pH 8.5, 10 mM TCEP, 50 mM chloroacetamide). Bottom-up experiments’ tryptic peptides were obtained by S-Trap Micro Spin Column according to the manufacturer’s protocol (Protifi, NY, USA). Briefly: Proteins were digested during 14 h at 37°C with 1 μg Trypsin sequencing grade (Promega). The S-Trap Micro Spin Column was used according to the manufacturer’s protocol. After speed-vacuum drying, eluted peptides were solubilized in 10 μL of 10% acetonitrile and 0.1% trifluoroacetic acid (TFA).

Liquid Chromatography-coupled Mass spectrometry analysis (LC-MS) analysis was done with similar parameters to the LFQ analysis of the WCL (see previous section), except the peptide separation run time was 60 min, ion accumulation and ramp time were 100ms, and precursors picking for MS/MS: 2,500 arbitrary units (a.u.).

The parameters for protein quantification and comparison were the same as for the LFQ analysis of the WCL, excepted for the MBR option that was not run (see previous section), and for the statistical test used (paired T test). The mass spectrometry proteomics data have been deposited to the ProteomeXchange Consortium via the PRIDE partner repository with the dataset identifiers PXD040862 (WCL) and PXD040855 (LysoIP).

Proteomic and RNAseq enrichment analysis

Enrichment analysis of the proteomic and RNAseq experiments were performed using g:Profiler[57] (version e107_e.g.,54_p17_bf42210) applying a significance threshold of 0.05. The Panther classification system[27] was also used to identify the main GO:function enriched in the proteomic analysis.

QUANTIFICATION AND STATISTICAL ANALYSIS

Densitometry and imaging quantifications were performed using the ImageJ software. All graphs were mounted and statistically tested using Prism 9. Unless otherwise specified, error bars on graphs are shown as mean ± s.e.m. of at least three independent biological replicates. A p value of <0.05 was considered significant. The RNAseq experiment was performed on three independent biological replicates. All proteomics experiments were performed on four independent biological replicates. Viability assays were performed on three independent experiments, each in triplicate.